Artificial neural network enhanced plasticity modelling and ductile fracture characterization of grade-1 commercial pure titanium

Abrar Salam Ebrahim , Qi Zhang , Jinjin Ha

PII: S0749-6419(24)00171-2
DOI: https://doi.org/10.1016/j.ijplas.2024.104044
Reference: INTPLA 104044

To appear in: *International Journal of Plasticity*

Received date: 29 February 2024
Revised date: 11 June 2024

Please cite this article as: Abrar Salam Ebrahim , Qi Zhang , Jinjin Ha , Artificial neural network enhanced plasticity modelling and ductile fracture characterization of grade-1 commercial pure titanium, *International Journal of Plasticity* (2024), doi: https://doi.org/10.1016/j.ijplas.2024.104044

Highlights

- Plasticity of CP-Ti is characterized with respect to strain rate and temperature
- ANNs can accurately describe strain hardening and plastic anisotropy of CP-Ti
- Differential hardening description enhances the ductile fracture predictions
- Ductile fracture models are calibrated with hybrid experiments and ANNs predictions

Artificial neural network enhanced plasticity modelling and ductile fracture characterization of grade-1 commercial pure titanium

by

Abrar Salam Ebrahim[a], Qi Zhang[b], Jinjin Ha[a]

Corresponding author: jinjin.ha@unh.edu

December 2023

[a] Department of Mechanical Engineering, University of New Hampshire, Durham, NH 03824, USA

[b] Department of Mathematics and Statistics, University of New Hampshire, Durham, NH 03824, USA

Abstract

This study primarily aims to develop a robust modelling approach to capture complex material behavior of CP-Ti, appeared by high anisotropy, differential hardening due to anisotropy evolution, and flow behavior sensitive to strain rate and temperature, using artificial neural networks (ANNs). Plasticity is characterized by uniaxial tension and in-plane biaxial tension tests at temperatures of 0°C and 20°C with strain rates of 0.001 /s and 0.01 /s, and the results are used to calibrate the non-quadratic anisotropic Yld2000-3d yield function with respect to the plastic work. In order to predict the intricate plastic deformation with the temperature and strain rate effects, two distinct ANN models are developed; one is to capture the strain hardening behavior and the other to predict the anisotropic parameters in the chosen yield function. The developed ANN models predict an unseen dataset well, which is intermediate testing conditions at a temperature of 10°C and strain rate of 0.005 /s. The ANN models, being computationally stable and adhering to conventional constitutive equations, are implemented into a user material subroutine for the ductile fracture characterization of CP-Ti sheet using the hybrid experimental-numerical analysis. The favorable agreement between experimental data and numerical predictions, particularly using the ANN models with evolving anisotropic material parameters for the Yld2000-3d yield function, underscores the significance of differential hardening effect on the ductile fracture behavior and highlights the capabilities of ANN models to capture the complex plastic behavior of CP-Ti. The key parameters including stress triaxiality, Lode angle parameter, and equivalent plastic strain at the fracture location are extracted from the simulations, enabling the calibration of ductile fracture models, namely Johnson-Cook, Hosford-Coulomb, and Lou-2014, and construction of fracture envelopes.

Keywords: Fracture (A), Anisotropic material (B), Constitutive behavior (B), Finite elements (C), Artificial neural networks.

1. Introduction

Commercially pure titanium (CP-Ti) has gained immense use across diverse industries, such as aerospace, biomedical, and chemical, owing to its exceptional properties and performance. For example, in proton exchange membrane fuel cells (PEMFCs), the substitution of conventional graphite bipolar plates with CP-Ti has emerged as a compelling alternative, primarily attributable to its low weight, exceptional corrosion resistance, excellent electrical conductivity, and cost-effective manufacturability (Meng et al., 2022). Due to its hexagonal close-packed (HCP) crystal structure, alpha titanium exhibits low crystal symmetry, resulting in a limited number of slip systems and reduced strain hardening ability. These distinct features of titanium require special attention to avoid undesired failure during forming applications. Thus, extensive understanding on the material plastic behavior leading to failure is needed.

In micromechanics, the damage, which eventually leads to fracture, is often explained by the void evolution in three stages: micro-voids nucleate at vulnerable sites (e.g., second phase particles), grow or coalesce, and then ultimately lead to localized failure across a sheet of micro-voids (Hayden and Floreen, 1969; Gurland, 1972; Thomason, 1990). Based on the micromechanical approach, Gurson (1977) proposed a porous plasticity model, considering the void volume fraction as a damage indicator. Subsequently, the original Gurson model has been extended to consider factors, such as void nucleation and coalescence (Chu and Needleman, 1980; Tvergaard and Needleman, 1984), void shape and size effects (Gologanu et al., 1993; Pardoen and Hutchinson, 2000; Wen et al., 2005), strain hardening (Leblond et al., 1995) and plastic anisotropy (Liao et al., 1997; Grange et al., 2000; Benzerga et al., 2001; Benzerga and Besson, 2001). These models are classified as coupled fracture models as they integrate the damage parameter with the elastoplastic behavior of the material.

Alternatively, several fracture criteria have been developed to predict ductile fracture without explicitly modeling the void nucleation and growth, known as uncoupled ductile fracture models. These criteria propose that the fracture takes place at a point within a body when the weighted measure of damage indicator, e.g., accumulated plastic strain, reaches a critical value (Clift et al., 1990; Le Roy et al., 1981;

McClintock, 1968; Oh et al., 1979; Rice and Tracey, 1969). The Johnson-Cook model (Johnson and Cook, 1985), which revealed a significant influence of stress triaxiality η on the initiation of fracture, has been widely utilized in various studies owing to its straightforward formulation. However, classical ductile fracture models lack the flexibility in describing fracture across a wide range of stress triaxialities η (Bao and Wierzbicki, 2004a).

Subsequently, ductile fracture models that incorporate the Lode angle parameter $\bar{\theta}$, which is a function of second and third invariants of the deviatoric stress tensor, have been introduced (Bai and Wierzbicki, 2008; Brünig et al., 2013, 2008; Lou and Yoon, 2017; Mirone and Corallo, 2010; Roth and Mohr, 2016; Wierzbicki et al., 2005). Bai and Wierzbicki, (2010) proposed a ductile fracture criterion for metals, known as modified the Mohr-Coulomb (MMC) model, by transforming the Mohr-Coulomb (MC) criterion into the space of equivalent plastic strain $\bar{\varepsilon}_f$, stress triaxiality η, and Lode angle parameter $\bar{\theta}$. Mohr and Marcadet (2015) made further advancements to the MMC model by substituting the Tresca equivalent stress for the Hosford equivalent stress, resulting in the development of the Hosford-Coulomb (HC) fracture model. Lou et al. (2014) also introduced a novel criterion utilizing a proposed changeable cut-off value function for the stress triaxiality η. Recently, Baral et al. (2024) proposed a new ductile fracture criterion that is capable of capturing fracture anisotropy by coupling DF2016 criterion with the non-quadratic Yld91 yield function. Additionally, various uncoupled fracture criteria have been developed, considering the influence of plastic work and elastic work (Khan and Liu, 2012a), strain rate and temperature (Khan and Liu, 2012b), volume change work and distortion work (Peng et al., 2021), as well as various void deformation modes (Zheng et al., 2023).

To characterize the fracture for various stress states, several experimental methods, such as notched tension, center hole, shear, punch, plane strain bending, in-plane biaxial tension, etc., have been implemented (Ha et al., 2019a; Habib et al., 2019). However, measuring damage parameters through experiments is challenging due to the three-dimensional stress states and inhomogeneous deformation fields near the fracture zones, as well as the difficulty in detecting crack initiation at the midplane through the sheet thickness. To overcome these limitations, researchers have adopted a hybrid experimental-numerical approach for ductile fracture analyses (Bai and Wierzbicki, 2008; Baral et al., 2019; Dunand and Mohr, 2010; Ha et al., 2018, 2019a; Luo et al., 2012; Mohr and Henn, 2007; Mu et al., 2020), where relevant variables are determined through numerical simulations. However, it is important to choose a suitable constitutive model to capture the anisotropy of plasticity leading to failure (Ha et al., 2020; Ha and Korkolis, 2021) in order to minimize the uncertainties from the finite element (FE) simulations and to achieve accurate prediction of critical parameters for the fracture model calibration, e.g., von Mises istropic yield function (Bao and Wierzbicki, 2004b; Li et al., 2010; Li and Wierzbicki, 2010) for isotropic materials and Hill 1948 anisotropic yield function (Beese et al., 2010; Dunand and Mohr, 2010; Wang et al., 2014) and Yld2004-18p (Ha et al., 2018, 2019a) for anisotropic materials. However, the Hill 1948 model falls short in providing satisfactory descriptions for both stress and r-value simultaneously, necessitating the non-associated flow rule. Advanced plastic anisotropy models, such as Yld2000-2d (Barlat et al., 2003), Yld2004-18p (Barlat et al., 2005), Banabic (Banabic, 2010), etc. have been introduced for advanced characterization of plastic anisotropy. The constitutive modelling of CP-Ti is considered challenging due to its complex behavior, including the significant anisotropy of flow stress and r-values, differential hardening, and tension and compression asymmetry, so called strength differential (SD) effect. Anisotropy in CP-Ti even shows strong evolution with respect to the strain, which is much severe than steel (Feng et al., 2021; Lee et al., 2016; Mamros et al., 2022) and aluminum alloys (Ha et al., 2018). Zhai et al. (2016) utilized the asymmetric CPB-06 yield function (Cazacu et al., 2006) for ductile fracture investigation of CP-Ti, whereas Baral et al. (2018) yielded the best prediction of experimental results for CP-Ti using KYL-12 (Khan et al., 2012) and CPB-06 yield functions. Additionally, Nagano et al. (2018) have successfully captured the plastic deformation behavior of CP-Ti using the Yld2000-2d model while Peters et al. (2014) incorporated the equivalent plastic strain and strain rate dependency to Yld2000-2d and validation with FE simulation of deep drawing process demonstrated significant improvement in the prediction accuracy. Complex plastic behavior of CP-Ti often requires intricate meso-scale modeling approach such as crystal plasticity and visco-plastic self-consistent formulation (Jeon et al., 2024; Tang et al., 2023; Wronski et al., 2018; Wroński et al., 2022, Lebensohn et al., 2007; Lebensohn and Tomé, 1993;

Wang et al., 2013), to study the deformation mechanisms with twinning, texture evolution, and associated behavior of CP-Ti.

Recently, machine learning based material modeling has emerged as a promising alternative to traditional physics based constitutive models. There are several attempts to develop machine learning based constitutive models that entirely replace the conventional mathematical framework (Bonatti and Mohr, 2022, 2021; Gorji et al., 2020; Kim et al., 2024; Mozaffar et al., 2019; Muhammad et al., 2021; Tasdemir et al., 2023; Zhang and Mohr, 2020), but some have also been exploring hybrid models, where neural network algorithms are integrated into existing physics based plasticity models (Fazily and Yoon, 2023; Jang et al., 2021; Jordan et al., 2020; Li et al., 2023, 2019; Liu et al., 2023; Pandya et al., 2020; Weber et al., 2023). Mozaffar et al. (2019) proposed a recurrent neural network (RNN) to capture plasticity behavior of a material. The model predicted complex phenomena, such as yield locus evolution with distortional hardening under 0.5% scaled mean absolute error (SMAE). Similarly, Zhang and Mohr (2020) developed a fully connected feedforward neural network to capture elasto-plastic response of a von Mises material and implemented within a FE framework for notched tension test. Additionally, Schmidt and Hartmaier (2023) presents a new texture descriptor for machine learning based constitutive modeling that effectively captures the structure-property relationship between texture and anisotropic plastic behavior. Moreover, Muhammad et al. (2021) proposed a machine learning framework that integrates additive manufacturing methods and artificial intelligence to predict the heterogeneous local strain observed during the plastic deformation of an additively manufactured aluminum alloy. However, the prediction accuracy and success of such data-driven approaches heavily relies on the quality and quantity of training data. Challenges arise if they do not adequately represent material behavior due to uncertainties or inaccuracies in physics based constitutive laws during the training (Bessa et al., 2017; Bessa and Pellegrino, 2018).

On the other hand, several researchers have adopted neural networks to effectively describe the temperature and strain rate dependency of material behaviors such as stress-strain response, strain aging, and fracture initiation. For instance, Li et al. (2019) modified the Johnson-Cook plasticity model by incorporating the effect of temperature and strain rate on the hardening of DP800 steel using a neural network through a hybrid experimental-numerical method. In a similar study, Jordan et al. (2020) was able to describe the temperature and strain rate dependent large strain response of a non-metallic material, i.e., polypropylene, using a shallow neural network with just one hidden layer. Li et al. (2022) introduced a counter example guided neural network with a state variable called effective aging time to separate the positive rate effects on viscous flow and negative rate effects on dynamic strain aging. Furthermore, by employing physics based assumptions and leveraging experimental data on fracture, Pandya et al. (2020) developed a neural network based fracture initiation model to address the significant influences of temperature, strain rate, and stress state on the failure behavior of aluminum 7075 during hot forming. However, the model was trained using a Hosford-Coulomb fracture model that did not account for varying temperature and strain rate. To address this limitation, Li et al. (2023) employed a neural network to extend the Hosford-Coulomb fracture criterion into the domain of strain rate and temperature.

This study primarily aims to develop a robust modelling approach to capture complex material behavior of CP-Ti, appeared by high anisotropy, differential hardening due to anisotropy evolution, and flow behavior sensitive to strain rate and temperature, using artificial neural networks (ANNs). Many past works on machine learning-based material modeling employ purely data-driven, statistical approaches. As a result, they do not strictly follow plasticity theories and may compromise computational stability when used for FE simulations. In contrast, hybrid approaches combine the machine learning algorithm with constitutive models developed within plasticity theory framework, e.g., hardening laws, yield function. This allows them to leverage the strengths of both machine learning and plasticity theory based models, such as robustness of machine learning, compatibility and numerical stability with FE simulations of plasticity theory based models. In addition, present work proposes an approach that is highly flexible for use with any plasticity models, chosen depending on material characteristics, (e.g., Bauschinger effect, strength differential effect, plastic anisotropy, etc.), and applications of interest, (e.g., springback with cyclic loading (Lee et al., 2018, 2012), ductile fracture (Ha et al., 2019b), hole flangeability (Ha and Korkolis, 2021)), etc.

Two independent artificial neural networks (ANNs) are developed and trained using experimentally generated data from uniaxial tension and biaxial tension tests to capture the strain hardening and plastic anisotropy of the material at various temperatures, strain rates, and plastic deformation levels. The ductile fracture of CP-Ti (grade 1) is investigated within the positive triaxiality range by a hybrid experimental-numerical approach, where the ANN models proposed for capturing the plasticity is incorporated with the uncoupled ductile fracture models. This also provides a validation for the proposed ANNs at an unseen temperature and strain rate condition. The strain to fracture is assessed experimentally for uniaxial tension, biaxial tension, plane strain tension, and shear conditions using specific specimen geometries suggested in the literature. The FE simulations of fracture experiments are performed using Abaqus/Implicit with ANN models incorporated into a user material (UMAT) subroutine and validated against the fracture experiments. Using the parameters obtained from the FE simulations, Johnson-Cook, Hosford-Coulomb, and Lou-2014 fracture initiation criteria are calibrated, and the fracture envelopes are constructed accordingly.

2. Plasticity Characterization

The material used in this study is commercially pure titanium (CP-Ti) in grade 1 received as 0.9 mm thick sheets of size 1.5 m x 1.2 m. The plasticity of material is characterized by uniaxial tension and biaxial tension tests to calibrate the Swift-Voce hardening model and Yld2000-3d yield function parameters (Dunand et al., 2012).

2.1 Uniaxial tension

The study employs ASTM E8 standard specimens machined using an abrasive water jet with orientations along the rolling direction (RD), 45° to the RD (referred to as diagonal direction, DD), and transverse direction (TD) as shown in Figure 1a. The tests are performed on a 250kN MTS landmark 370 servo-hydraulic universal testing machine with crosshead speeds set at 0.1 mm/s and 1 mm/s to achieve strain rates of approximately 0.001 /s and 0.01 /s, respectively, in the gauge section. For each strain rate case, the tests are carried out at two different temperatures, 20°C and 0°C. At least 3 samples are tested for each condition for repeatability. To ensure uniform temperature across the gage area during the tests, a cooling plate of 150 mm × 200 mm is affixed to the specimens from the rear side. A silicon based thermal paste with thermal conductivity of 0.735 W/mK is applied to the specimen and cooling plate interface for effective heat transfer between them.

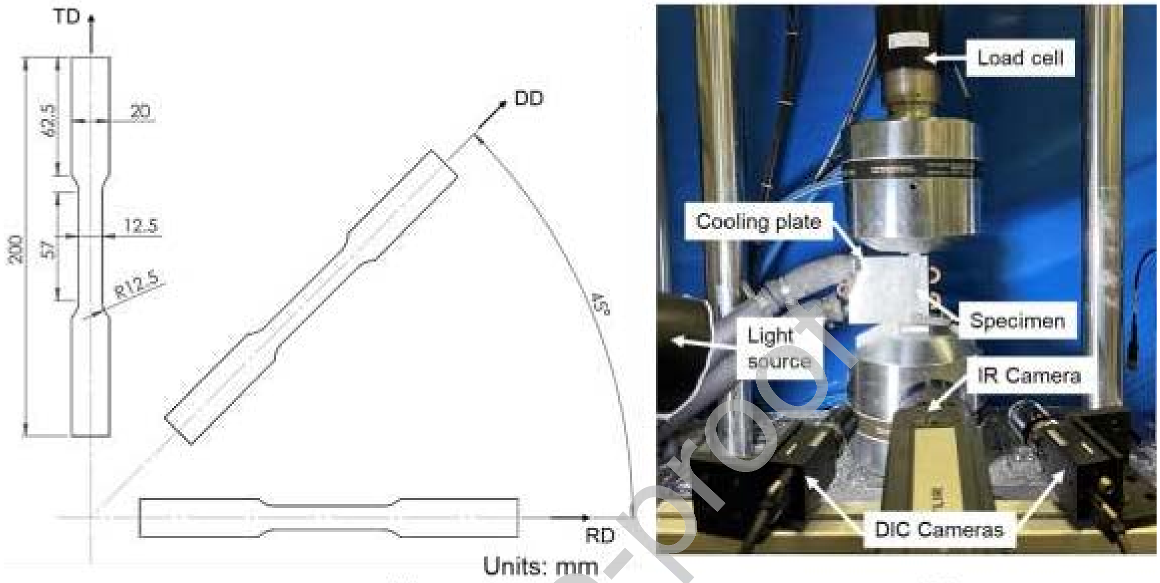

(a) (b)

Figure 1 a) ASTM E8 specimen along RD, DD, and TD and b) experimental setup in MTS with stereo-DIC, IR camera, and cooling plate for temperature controlled uniaxial tension test.

A random black speckle on a white background is spray painted onto the sample surfaces to capture the strain field using a stereo type digital image correlation (DIC) system. The stereo-DIC system consists of two 9 MP cameras (Grasshopper3 89S6M) and a light source for the full strain field measurement and an infrared (IR, FLIR SC645) camera for the temperature field (see Figure 1b). The images are captured at acquisition rates of 12.5 Hz and 2 Hz for tests conducted at strain rates of 0.01 /s and 0.001 /s, respectively. The stereo-DIC system is synchronized with the MTS load cell to ensure accurate correlation between load and strain data. The DIC images have a resolution close to 0.035 mm/pixel. Post-processing of the captured images is performed using VIC-3D software, with a filter size of 5, subset of 29 pixels, and step size of 7 pixels for strain and temperature distribution analysis.

2.2 Biaxial tension

The in-plane biaxial tension tests are performed using cruciform samples fabricated using the abrasive water jet. The specimen arms are aligned in the RD and TD of the material and contain 5 equally spaced slits as shown in Figure 2a. The center of the specimen is carefully machined down to 0.4 mm thickness using an end mill on both sides of the sample. The tests are carried out using a displacement control tabletop biaxial loading frame developed at the University of New Hampshire (UNH) as shown in Figure 2b (Wilson et al., 2013). Hydraulic cylinders with a stroke of 12.7 mm and tensile force capacity of 25.8 kN load the samples. An equibiaxial displacement path $(\delta_x\colon\delta_y = 1\colon1)$ is programmed to load the cruciform specimens at crosshead speeds close to 0.2 mm/s and 0.02 mm/s to achieve 0.01 /s and 0.001 /s strain rates, respectively, at the center square gauge area. Air streams from two vortex tubes with inlet pressures set at 827 kPa are directed towards the gage area to control the surface temperature. The airflow at the vortex tube outlets is adjusted such that uniform temperatures of 20°C and 0°C are obtained at the gage surface during the tests. A stereo-DIC system with two 5 MP Grasshopper (GRAS-50S5M) cameras and the FLIR IR camera are mounted on a metallic frame attached to the machine, to capture the strain and temperature fields at the gage area. The acquisition rate is set at 2 Hz, and the images are postprocessed using VIC-3D software with the same parameters as in the uniaxial tension tests.

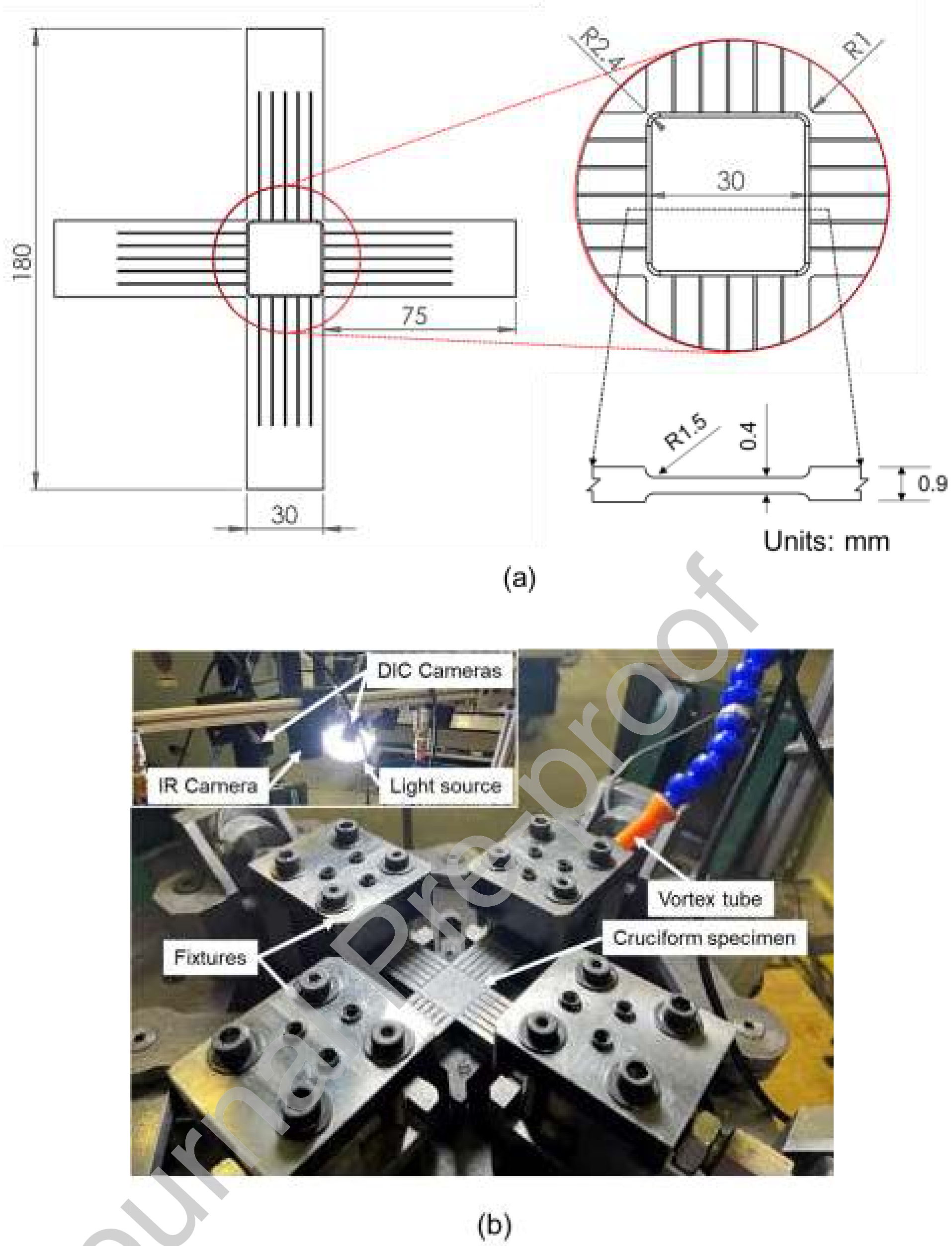

Figure 2 a) Cruciform specimen geometry and b) in-plane biaxial tension test setup with stereo-DIC, IR camera, and vortex tube for temperature control.

2.3 Plastic anisotropy

The engineering stress-strain curves shown in Figures 3a and 3b demonstrate the effect of orientation, temperature, and strain rate on the mechanical behavior of CP-Ti (grade 1). The three distinct orientation curves, i.e., RD, DD, and TD, for each temperature and strain rate condition depict the anisotropy in the flow stress. The yield strength measured with the 0.2% offset method is found to be the highest in the

TD, which agrees with the available literature on the mechanical behavior of CP-Ti (Baral et al., 2018; Pham et al., 2019; Roth et al., 2014). Across all orientations, higher strength is observed at lower temperature and higher strain rate. The samples tested along the RD have superior ductility and strength, whereas the DD and TD result in low uniform elongation, i.e., plastic strain prior to the peak engineering stress, and high post-necking deformation, i.e., strain after the peak engineering stress. For the 20°C and 0.001 /s condition, the ratio of the uniform to the total elongation in the RD, DD, and TD are 0.62, 0.19 and 0.28, respectively.

Furthermore, the work hardening rates in each orientation exhibit visually distinguishable variations within the range of uniform deformation. The anisotropy of flow stress in this material is possibly related to twinning of CP-Ti (Yi et al., 2016). The twinning activity is controlled by material grade, specifically oxygen content (Choi et al., 2021), deformation type, such as tensile/compressive (Yang et al., 2022; Yi et al., 2016), material orientation (Battaini et al., 2007; Pham et al., 2019; Yi et al., 2016), and initial grain size (Deguchi et al., 2023). Temperature is also a significant factor governing the twinning volume fraction and the active twin systems (Yang et al., 2022).

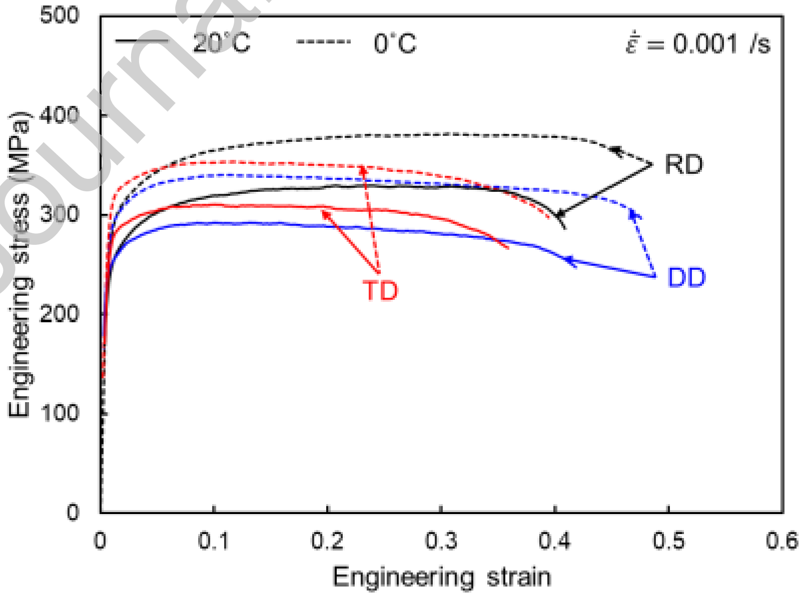

(a)

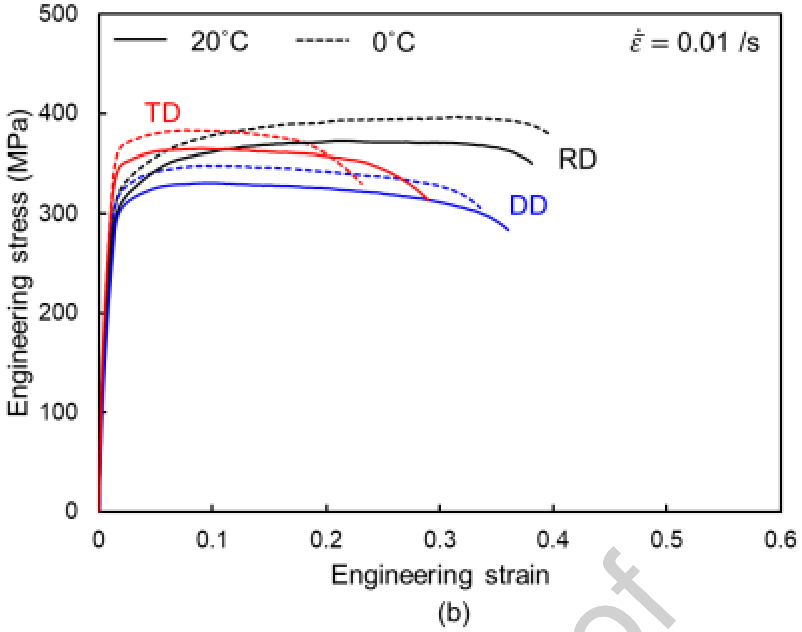

Figure 3 Engineering stress-strain curves of uniaxial tension in RD, DD, and TD at strain rates of (a) 0.001 /s and (b) 0.01 /s.

Figures 4a and 4b show the evolution of normalized stress $\hat{\sigma}$ with the plastic work W_p in the uniaxial tension and in-plane biaxial tension tests. Each flow stress is normalized by the reference condition, which is uniaxial tension in the RD in this study, i.e., $\hat{\sigma}_i = \sigma_i/\sigma_{RD}$. During the early stages of plastic deformation, the normalized stresses of DD and TD, i.e., $\hat{\sigma}_{DD}$ and $\hat{\sigma}_{TD}$, are greater than 1, which eventually become lower than 1 as the plastic work progresses. This means that the flow stresses in the uniaxial tension in the DD and TD are initially higher than the RD and decreased with reduced hardening rate. Similarly, the evolutional behavior in the biaxial tension along the RD and TD, i.e., $\hat{\sigma}_{b,RD}$ and $\hat{\sigma}_{b,TD}$, is observed, but the values always exceed 1. The observed evolution in the flow stress anisotropy appears as differential hardening, which is indicated by the non-uniform expansion of the yield locus, under various proportional loading conditions.

Figures 5a and 5b show the evolution of strain ratio with plastic work W_p. The strain ratio in uniaxial tension is defined by the Lankford coefficient, so called r-value, which is the ratio of plastic strain increments in the width to the thickness directions, i.e., $r = d\varepsilon_w/d\varepsilon_t$. For biaxial tension, it is defined as the ratio of plastic strain increments in the TD to the RD, i.e., $r_b = d\varepsilon_{TD}/d\varepsilon_{RD}$, which represents the tangential slope of the yield locus in biaxial tension. The anisotropy observed in the r-values and r_b is more pronounced compared to the anisotropy in flow stress. In uniaxial tension, the r-value variation Δr in CP-Ti is significant compared to other lightweight materials, such as steel and aluminum alloys: r_{TD} exhibits the highest value, then r_{DD} followed by r_{RD}. In addition, the significant evolution is observed at the beginning of plastic work and quickly saturated to a constant level which is close to the average strain ratio, i.e., $r = \varepsilon_w/\varepsilon_t$, in the homogeneous deformation range.

The evolution of experimentally obtained stresses (normalized flow stresses) and strain ratios (r-value and r_b) with respect to the plastic work W_p are approximated using an exponential function,

$$y_{fit} = \omega_1 \cdot \exp(\omega_2 \cdot W_p) + \omega_3 \cdot \exp(\omega_4 \cdot W_p) \qquad (1)$$

which is later used for the yield function parameter calibrations. The coefficients $\omega_{i,1-4}$ in Eq. (1) are found by fitting experiment data, as in Figures 4 and 5. It is assumed that the plastic anisotropy is saturated as the plastic deformation increases and does not change beyond the plastic work level of 45 MJ/m^3.

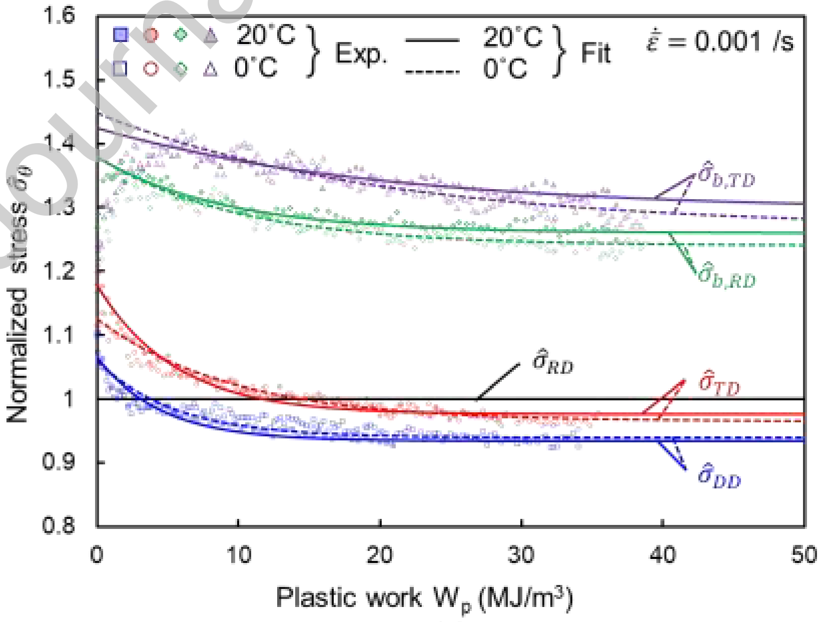

(a)

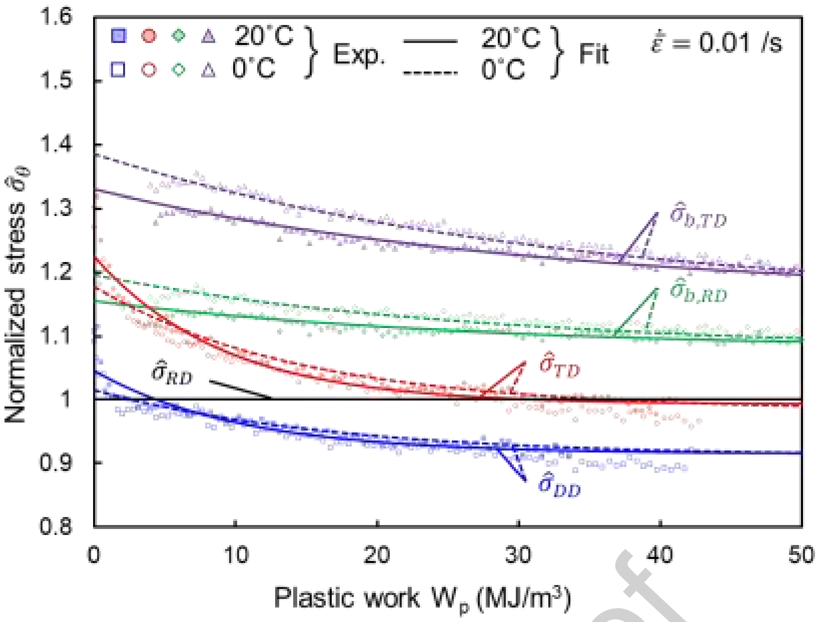

(b)

Figure 4 Evolution of normalized stress with respect to plastic work W_p at strain rates of (a) 0.001 /s and (b) 0.01 /s.

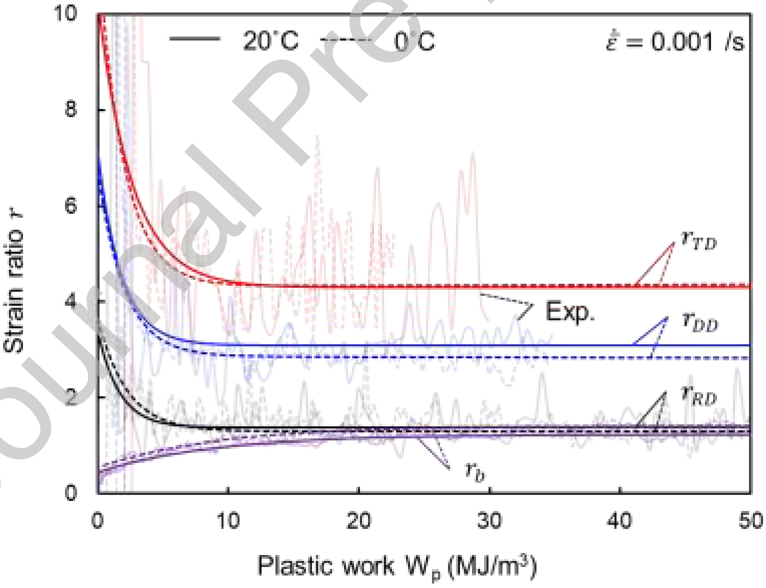

(a)

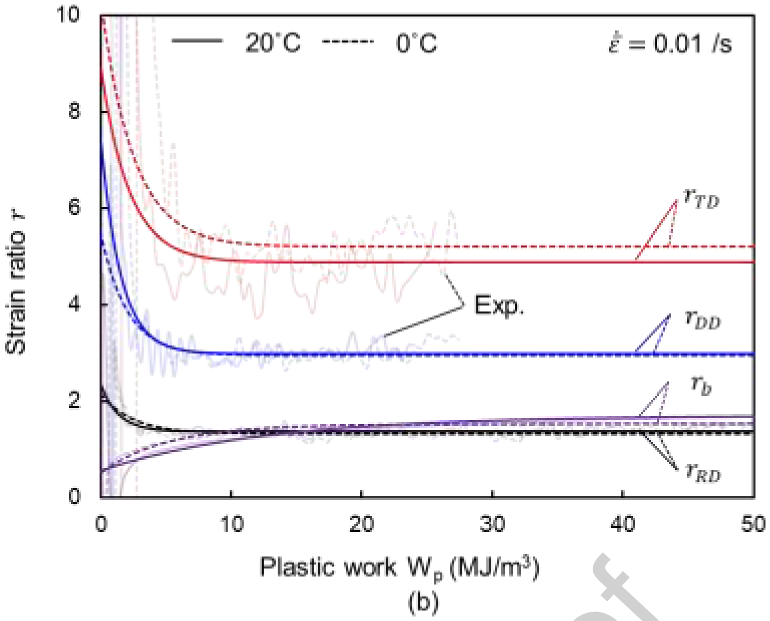

(b)

Figure 5 Evolution of strain ratio with respect to plastic work W_p at strain rates of (a) 0.001 /s and (b) 0.01 /s. The transparent curves in the background represent experimental results, and the dark curves represent exponential fitting.

3. Constitutive modelling of CP-Ti

According to classical plasticity theory, deformation is governed by,

$$F(\boldsymbol{\sigma}, \bar{\varepsilon}) = \phi(\boldsymbol{\sigma}) - H(\bar{\varepsilon}) = 0 \tag{2}$$

where $\phi(\boldsymbol{\sigma})$ is the equivalent stress defined by the yield function of Cauchy stress tensor $\boldsymbol{\sigma}$ and $H(\bar{\varepsilon})$ is the flow stress from the strain hardening model as a function of equivalent strain. Assuming that the plastic potential and yield functions are identical, the plastic strain increment is determined by the associated flow rule as follows,

$$d\boldsymbol{\varepsilon}^{\boldsymbol{p}} = d\lambda \frac{\partial F}{\partial \boldsymbol{\sigma}} \tag{3}$$

where $d\lambda$ is a plastic multiplier. The present work follows the above classical plasticity theory while two deep learning models are employed to capture the strain hardening $H(T, \dot{\bar{\varepsilon}}, \bar{\varepsilon})$ and the plastic anisotropy evolution with respect to yield function parameters $\alpha\left(T, \dot{\bar{\varepsilon}}, W_p\right)$ at various temperatures and strain rates.

3.1 Hardening law

In order to extrapolate the hardening behavior, the combined Swift-Voce hardening law (Dunand and Mohr, 2010) is used to describe the stress-strain response of the material. The flow stress given by the Swift-Voce hardening law is,

$$H(\bar{\varepsilon}) = \bar{\sigma} = w_{sv} \cdot \sigma_{Swift} + (1 - w_{sv}) \cdot \sigma_{Voce} \tag{4}$$

where $\sigma_{Swift} = s_0 \cdot (s_1 + \bar{\varepsilon})^{s_2}$ and $\sigma_{Voce} = v_0 - v_1 \cdot \exp(-v_2 \cdot \bar{\varepsilon})$ with w_{sv} for the weight factor and $s_{i,0-2}$ and $v_{i,0-2}$ for material parameters (see Appendix A). The parameters are calibrated with the stress-strain curve of uniaxial tension in the RD. The Swift-Voce curve fittings at two strain rates (0.01 /s and 0.001 /s) and three temperatures (-10˚C, 0˚C and 20˚C) can be found in Figure 6. The additional set of uniaxial tension tests conducted at a temperature of -10°C and strain rates of 0.001 /s and 0.01 /s are aimed to enhance the diversity of the training dataset for the strain hardening artificial neural network (ANN) model, which is discussed in section 4.2.

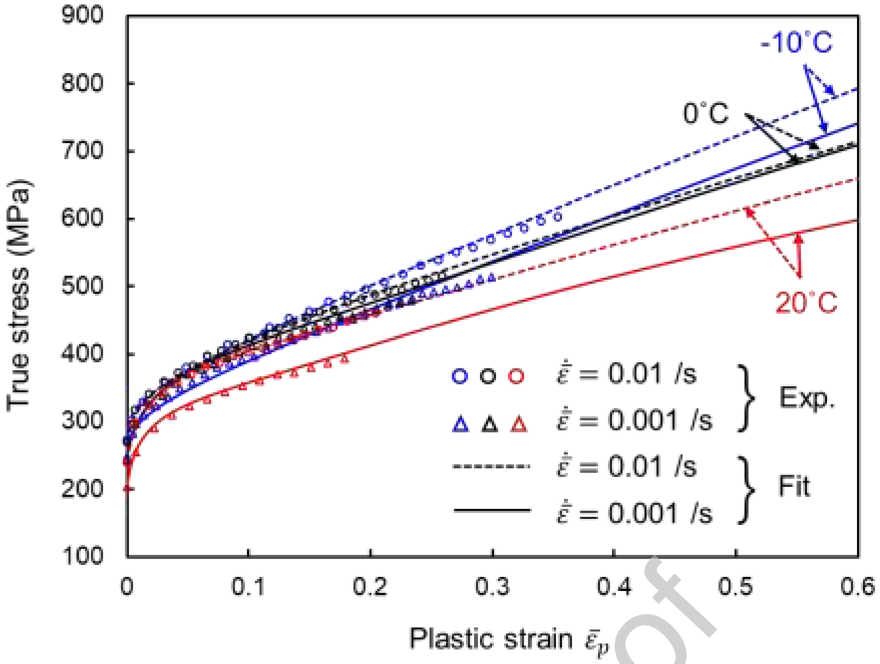

Figure 6 Identification of Swift-Voce hardening curves at two strain rates (0.01 /s and 0.001 /s) and three temperatures (-10˚C, 0˚C and 20˚C).

3.2 Anisotropic yield function

As the local stress and strain parameters are obtained from the FE simulation in the hybrid approach, it is important to achieve the accurate prediction of plastic deformation of the anisotropic material. To capture plastic anisotropy and its evolution in response to plastic work, this study employs a non-quadratic anisotropic yield function Yld2000-3d (Dunand et al., 2012). This is an extended version of Yld2000-2d (Barlat et al., 2003) model from plane stress to a full 3D stress condition without additional anisotropic material parameters, i.e., $\alpha_{i,1-8}$. It should be noted that Yld2004-18p (Barlat et al., 2005) for a full stress condition has 18 parameters for anisotropy description, which can be reduced to 16 independent parameters (Van Den Boogaard et al., 2016). Yld2000-3d has similar mathematical formulations with the original Yld2000-2d model as,

$$\phi = \phi'(\boldsymbol{s}') + \phi''(\boldsymbol{s}'') = 2\bar{\sigma}^n \tag{5}$$

where $\phi'(\boldsymbol{s}') = |S_1' - S_2'|^n$ and $\phi(\boldsymbol{s}'') = |2S_1'' + S_2''|^n + |S_1'' + 2S_2''|^n$. n is the yield function exponent related to the crystal structure, e.g., 6 for body- and 8 for face-centered cubic. The (S_1', S_2') and (S_1'', S_2'') in the above expression are the principal values of the deviatoric stress tensors $\boldsymbol{s}'$ and $\boldsymbol{s}''$, which are linearly transformed Cauchy stress $\boldsymbol{\sigma}$ by operators $\boldsymbol{L}'$ and $\boldsymbol{L}''$as,

s

$$\boldsymbol{s}' = \boldsymbol{C}'\boldsymbol{s} = \boldsymbol{C}'\boldsymbol{T}\boldsymbol{\sigma} = \boldsymbol{L}'\boldsymbol{\sigma} \tag{6}$$

$$\boldsymbol{s}'' = \boldsymbol{C}''\boldsymbol{s} = \boldsymbol{C}''\boldsymbol{T}\boldsymbol{\sigma} = \boldsymbol{L}''\boldsymbol{\sigma} \tag{7}$$

Tensor representation of two linear transformation tensors $\boldsymbol{L}'$and $\boldsymbol{L}''$ of Yld2000-3d anisotropic yield function (Dunand et al., 2012), used to transform the Cauchy stress $\boldsymbol{\sigma}$ to deviatoric stress tensors $\boldsymbol{s}'$and $\boldsymbol{s}''$are given as:

$$\boldsymbol{L}' = \frac{1}{3}\begin{bmatrix} 2\alpha_1 & -\alpha_1 & -\alpha_1 & 0 & 0 & 0 \\ -\alpha_2 & 2\alpha_2 & -\alpha_2 & 0 & 0 & 0 \\ 0 & 0 & 0 & 3\alpha_7 & 0 & 0 \\ 0 & 0 & 0 & 0 & 3\alpha_9 & 0 \\ 0 & 0 & 0 & 0 & 0 & 3\alpha_{10} \end{bmatrix} \tag{8}$$

$$\boldsymbol{L}'' = \frac{1}{9}\begin{bmatrix} -2\alpha_3 + 2\alpha_4 + 8\alpha_5 - 2\alpha_6 & -4\alpha_4 + 4\alpha_6 + \alpha_3 - 4\alpha_5 & \alpha_3 + 2\alpha_4 - 4\alpha_5 - 2\alpha_6 & 0 & 0 & 0 \\ 4\alpha_3 - 4\alpha_4 - 4\alpha_5 + \alpha_6 & -2\alpha_3 + 8\alpha_4 + 2\alpha_5 - 2\alpha_6 & -2\alpha_3 - 4\alpha_4 + 2\alpha_5 + \alpha_6 & 0 & 0 & 0 \\ 0 & 0 & 0 & 9\alpha_8 & 0 & 0 \\ 0 & 0 & 0 & 0 & 9\alpha_{11} & 0 \\ 0 & 0 & 0 & 0 & 0 & 9\alpha_{12} \end{bmatrix} \tag{9}$$

The linear transformation tensors above are composed of 12 anisotropic material parameters $\alpha_{i,1-12}$, among which $\alpha_{i,9-12}$ represent out of plane shear stresses. These parameters are considered unity as the out of plane shear stresses are assumed to be isotropic, thereby reducing the computation cost (Dunand et al., 2012). The Cauchy stress vector is $\sigma = \{\sigma_{xx} \quad \sigma_{yy} \quad \sigma_{zz} \quad \sigma_{xy} \quad \sigma_{yz} \quad \sigma_{zx}\}$ and the transformed stress deviator vectors are $s' = \{s'_{xx} \quad s'_{yy} \quad s'_{xy} \quad s'_{yz} \quad s'_{zx}\}$ and $s'' = \{s''_{xx} \quad s''_{yy} \quad s''_{xy} \quad s''_{yz} \quad s''_{zx}\}$.

To capture the differential hardening behavior as shown in Figures 4a and 4b, the variations of normalized stresses ($\hat{\sigma}_{RD}$, $\hat{\sigma}_{DD}$, $\hat{\sigma}_{TD}$ and $\hat{\sigma}_b$) and strain ratios (r_{RD}, r_{DD}, r_{TD} and r_b) are fitted by an exponential equation as Eq. (1), and the results are used to calibrate the parameters with respect to the plastic work $\alpha_{i,1-8}(W_p)$. The parameters are determined by solving the equations using the least square algorithm consecutively with respect to the plastic work. Different values have been recommended for the yield function exponent n in the literature. For instance, Nagano et al. (2018) observed the closest agreement with the experimental data when n =8 is used to describe the anisotropy of a pure titanium sheet. In this study, The yield function exponent is set to n=8 based on the recommendation by Ishiki et al. (2011) for CP-Ti, identified using uniaxial tension and in-plane biaxial tension tests for the Yld2000-2d yield locus which should produce the same yield locus description with Yld2000-3d. However, there are other studies using different values of exponent based on the material, e.g., 6, 8, and 10, etc., (Hu et al., 2021; Mutrus et al., 2010).

The evolutionary parameters $\alpha_{i,1-8}(W_p)$, calibrated for different strain rate and temperature conditions up to a plastic work level of W_p=45 MJ/m³, are illustrated in the Figures 7a and 7b. Most parameters tend to saturate with the exception of α_2 and α_3 when W_p<30 MJ/m^3, and all the parameters are assumed to be constant when W_p>45 MJ/m^3. Figure 8 showcases the normalized yield loci predictions of CP-Ti by the calibrated $\alpha_{i,1-8}(W_p)$ parameters, under different levels of W_p for strain rates of 0.001 /s and 0.01 /s and temperatures of 0˚C and 20˚C. Representation of yield loci in the real stress space is shown in Figures B1(a) and (b) Appendix B. As discussed in Section 1, a strong differential hardening is observed in the yield loci plots, especially at small plastic work levels, and eventually stabilizes at a higher plastic work level, approximately 30 MJ/m^3.

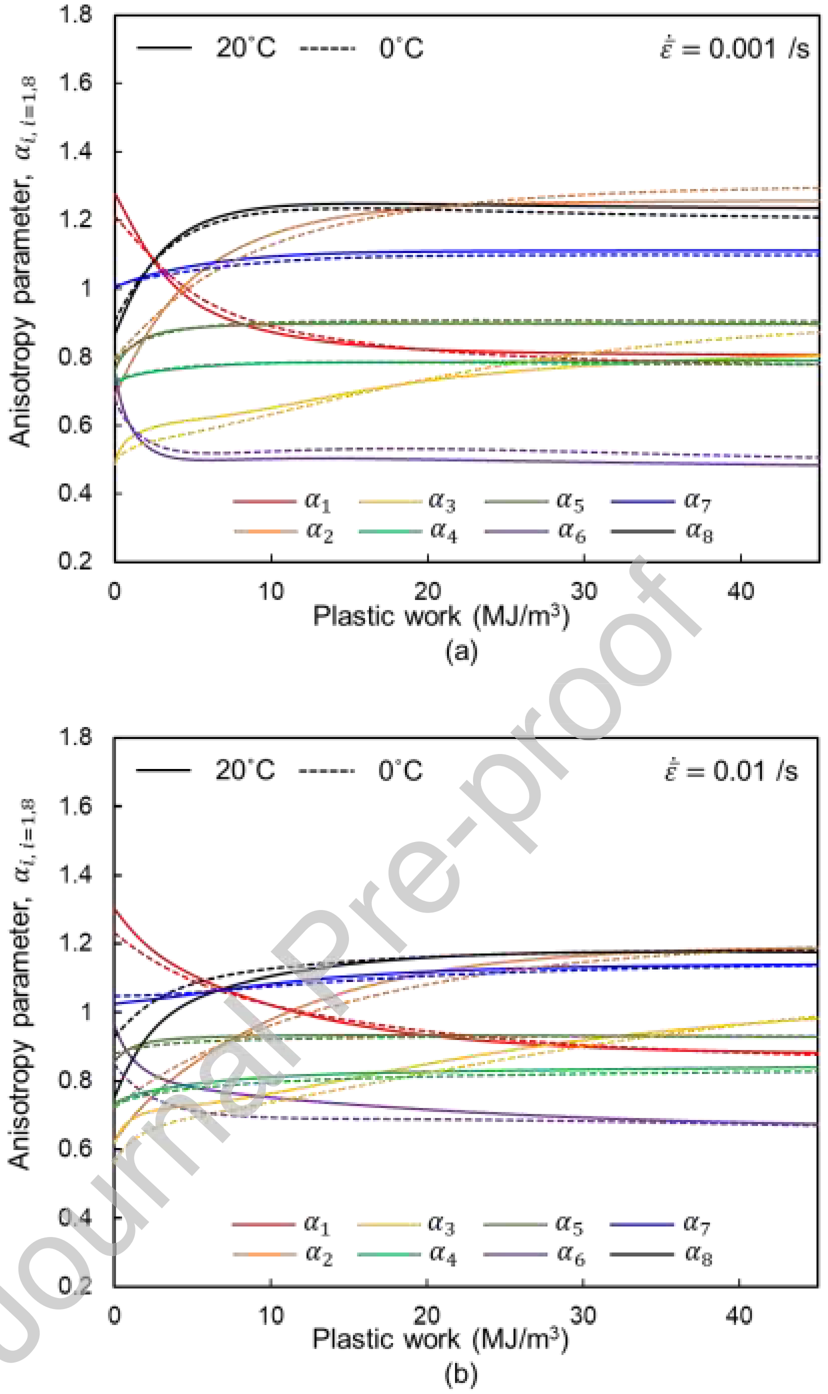

Figure 7 Yld2000-3d parameters calibrated for 0˚C and 20˚C at strain rates of (a) 0.001 /s and (b) 0.01 /s plotted with respect to plastic work W_p.

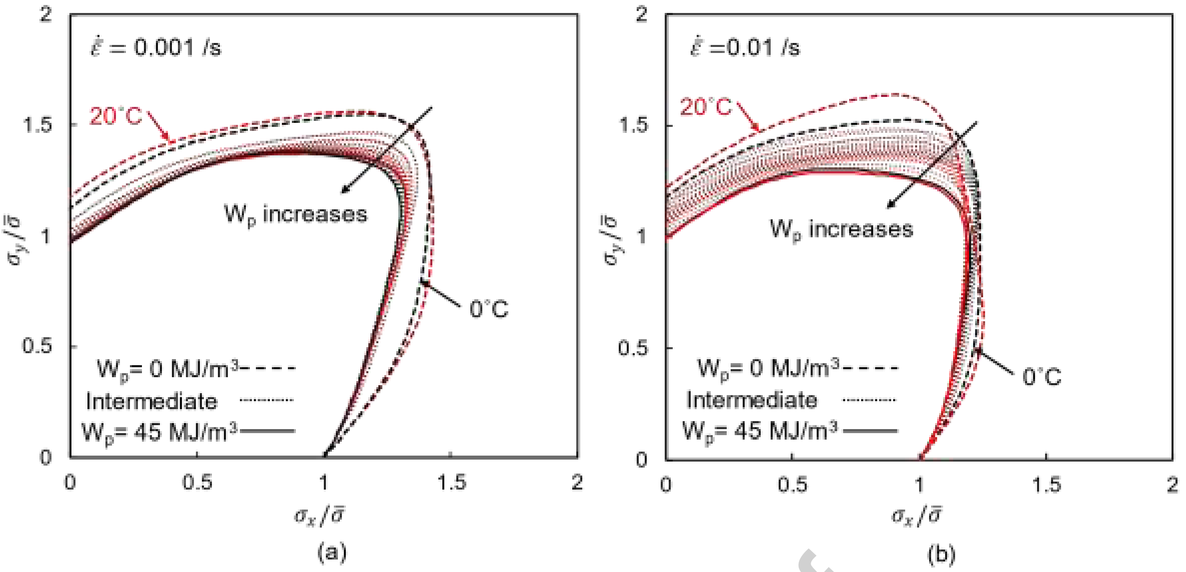

(a) (b)

Figure 8 Yield locus evolution in normalized stress space at strain rates of (a) 0.001 /s and (b) 0.01 /s.

The plasticity characterization of CP-Ti underscores the complexity of its yielding behavior which is influenced by factors such as material anisotropy, plastic deformation level, strain rate and temperature. It highlights the necessity of these multiple factors for an accurate description of the material's plasticity. While previous works have numerically implemented the strain rate dependency of anisotropic yield functions (Peters et al., 2014), we employ a robust approach with an ANN model employed within the Yld2000-3d framework to describe the strain rate and temperature dependent evolution of anisotropic yield locus for CP-Ti.

4. Artificial neural network (ANN) modeling

4.1 Architecture of ANN models

To address the complexity of plastic behavior of CP-Ti as shown in section 3, a robust material modeling approach that integrates the machine learning algorithm with constitute models developed within plasticity theory framework, is proposed. This method leverages the flexibility of machine learning algorithms while adhering to the conventional constitutive equations and thereby ensuring numerical stability of FE simulations. Specifically, two deep learning regression models are introduced to capture the effect of strain rate and temperature on the strain hardening and plastic anisotropy as a function of plastic deformation, i.e., equivalent plastic strain and plastic work. Deep learning involves training an ANN with multiple layers and nodes to learn to make predictions from the complex data.

ANNs are typically built of multiple layers, which consist of several nodes, to progressively extract complex features from the input. In many neural network architectures, these layers are structured in a sequential manner, forming a chain-like structure where each layer is a function of the preceding layer. The input data $\boldsymbol{X}$ is fed into an input layer and passes through several hidden layers. The neurons in different layers are connected via weights $\boldsymbol{W}$ and biases $\boldsymbol{b}$**,** enabling information flow throughout the network. An activation function is applied to the weighted sum of inputs to introduce non-linearity into the network. The final predictions $\boldsymbol{Y'}$ are made at the output layer.

For an ANN comprising l hidden layers, the mathematical representation for various layers can be summarized as,

- The output from the first hidden layer is,

$$\boldsymbol{Y_1} = \psi(\boldsymbol{W_1} \cdot \boldsymbol{X} + \boldsymbol{b_1}) \tag{10}$$

where $\boldsymbol{W_1}$ and $\boldsymbol{b_1}$ are the weight and bias matrices associated with the first hidden layer, $\boldsymbol{X}$ is the input vector of shape $(k \times 1)$ fed into the ANN when k is the number of inputs, and ψ is the activation function applied to each layer.

- In the subsequent hidden layers, the output of the previous layer serves as the input.

$$\boldsymbol{Y_{i=2,l}} = \psi(\boldsymbol{W_{i=2,l}} \cdot \boldsymbol{Y_{i=1,l-1}} + \boldsymbol{b_{i=2,l}}) \tag{11}$$

- Finally, the predictions from the ANN are given by the output layer,

$$\boldsymbol{Y'} = \boldsymbol{W_{op}} \cdot \boldsymbol{Y_l} + \boldsymbol{b_{op}} \tag{12}$$

where $\boldsymbol{W_{op}}$ and $\boldsymbol{b_{op}}$ are the weight and bias matrices of the output layer, respectively, $\boldsymbol{Y_l}$ is the output from the l^{th} hidden layer, and $\boldsymbol{Y'}$ is the output vector of the shape $(m \times 1)$ when m is the number of outputs from the ANN.

Being a regression problem, this study used mean-squared error (MSE) between the target value y_m and the ANN output y'_m as the cost function ξ.

$$\xi = \frac{\sum_{i=1}^{m}(y_i - y_i')^2}{m} \tag{13}$$

The objective of the training phase is to determine weight and bias matrices reducing the cost function, equivalently improving the prediction accuracy. The backpropagation algorithm is employed to compute the gradients of the cost function from the output layer back to the input layer. The gradients are subsequently used to update the weights and biases of each neuron using the gradient descent optimization method. During the prediction, flow of data is unidirectional from the input layer to the output layer through the hidden layers.

In the current study, two independent ANN models are proposed: ANN$(\bar{\sigma})$ to capture the strain hardening behavior and ANN(α) to capture the evolution of plastic anisotropy commonly existing in a CP-Ti sheet. The ANN$(\bar{\sigma})$ replaces conventional hardening models and predicts the stress as a function of temperature T, strain rate $\dot{\bar{\varepsilon}}$, and plastic strain level $\bar{\varepsilon}$. On the other hand, ANN(α) is introduced to predict the parameters of the Yld2000-3d yield function taking into account the temperature T, strain rate $\dot{\bar{\varepsilon}}$, and plastic work W_p, thereby describing the plastic anisotropy of CP-Ti within a classical yield function framework. This approach is aimed to enhance the robustness in modelling complex material behavior using machine learning algorithm while following the plasticity theory framework. The ANN models can be represented as,

$$\text{ANN}(\bar{\sigma}): \quad \begin{Bmatrix} T \\ \dot{\varepsilon} \\ \bar{\varepsilon} \end{Bmatrix} \rightarrow \{\bar{\sigma}\}$$

$$\text{ANN}(\alpha): \quad \begin{Bmatrix} T \\ \dot{\varepsilon} \\ W_p \end{Bmatrix} \rightarrow \begin{Bmatrix} \alpha_1 \\ \alpha_2 \\ . \\ . \\ \alpha_8 \end{Bmatrix}$$

When it comes to the architecture of the ANN model, important decisions involve determining the depth of the network (# of layers), width of each layer (# of nodes), and activation function. Deeper networks often exhibit the ability to achieve comparable generalization to the test set using fewer nodes per layer and thus fewer parameters. However, optimizing deeper networks can be more challenging. Therefore, the optimal network architecture for ANN (α) is determined using KerasTuner, a Python library for hyperparameter optimization. KerasTuner utilizes a random search algorithm to efficiently explores a wide range of hyperparameters, increasing the chance of finding an optimal solution and proposes the best architecture from the predefined search space. Subsequently, neural networks are developed in Python using Keras and TensorFlow libraries. The schematic diagram shown in Figure 9 illustrates the ANN architectures developed for this study.

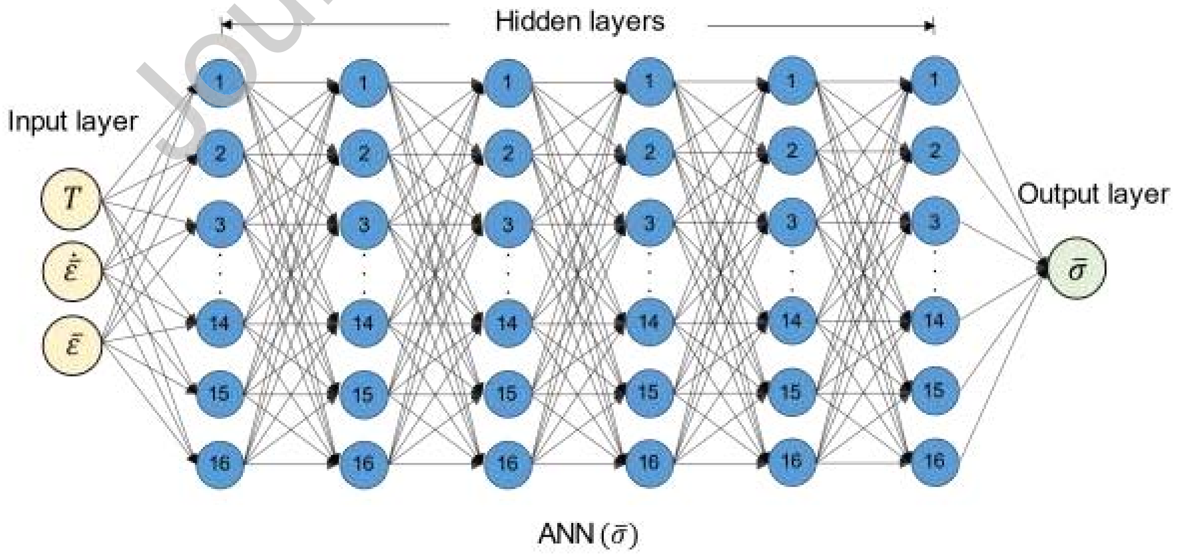

ANN $(\bar{\sigma})$

(a)

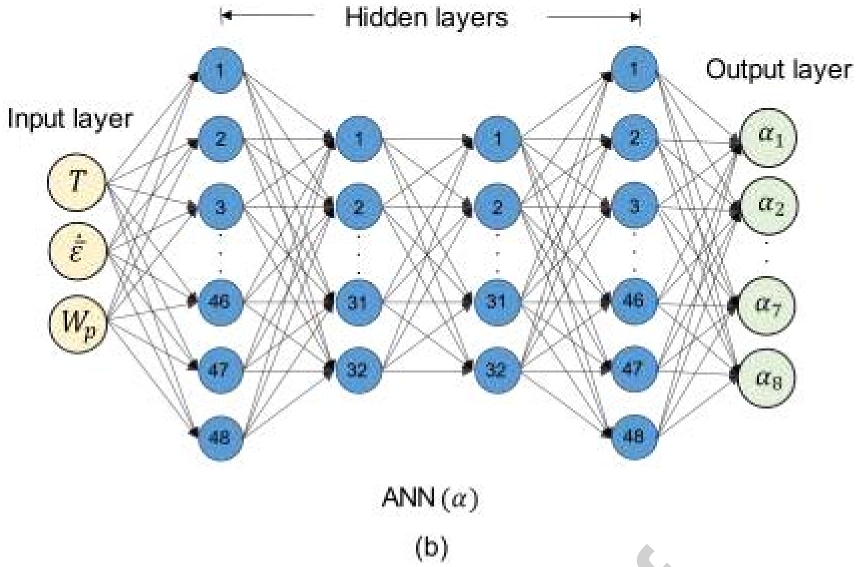

Figure 9 Schematic diagram showing architectures of (a) ANN($\bar{\sigma}$) and (b) ANN(α).

4.2 Training of ANN models

The construction of ANN involves several essential steps, including creating and preprocessing training data, determining the network architecture, and training the network. For the training of the ANN($\bar{\sigma}$), the six extrapolated hardening curves at three temperatures (-10, 0 and 20 ˚C) and at two strain rates (0.01 and 0.001 /s), as shown in the Figure 6, are used. The training dataset comprises a total of 6006 data points created by Swift-Voce fitting to the experiment with $\Delta\bar{\varepsilon} = 0.001$ between $0 \leq \bar{\varepsilon} \leq 1$. Similarly, a total of 18004 training data points are generated for the ANN(α) with a plastic work increment $\Delta W_p = 0.01$ between $0 \leq W_p \leq 45$ MJ/m^3. The input data are normalized using the following equation to eliminate any bias that could arise due to differences in the magnitudes of the different input features.

$$x_{norm} = \frac{x - x_{min}}{x_{max} - x_{min}} \tag{14}$$

where x_{max} and x_{min} are the maximum and minimum values of each input feature within the training data.

Among the total datasets, 15% is reserved as unseen to test the performances of the ANN($\bar{\sigma}$) and ANN(α) after training. For the ANN(α), additional 15% of the dataset is used for validation, leaving 70% of the dataset for training. Given the limited number of training data, K-fold cross-validation is employed for the ANN ($\bar{\sigma}$). In this technique, the dataset is divided into K equal-sized subsets, with one subset used for validation, leaving the remaining $K-1$ subsets for training. This process is repeated K times with each time a different subset used for validation, to ensure comprehensive validation of the model performance. With K=8 chosen as the optimal value; results are averaged to estimate the overall model performance. For the ANN(α), K-fold cross-validation is not required as sufficient training data is available. The Table 1 below provides an overview of features of ANN($\bar{\sigma}$) and ANN(α).

During the training of the ANN models, an early stopping criterion with a patience of 30 epochs is applied. This criterion monitors the model performance on the validation set throughout training and halts the process if the performance ceases to improve or degrades continuously for 30 consecutive epochs. Additionally, a callback named ModelCheckpoint is implemented to save the best-performing model, ensuring that the best model is saved rather than the model at the final epoch. These features are intended to prevent the model from over training. The learning curves demonstrating the performance evaluation of the ANN models during training and validation with respect to number of epochs are shown in Figure 10. The ANN($\bar{\sigma}$) and ANN(α) achieved remarkable performance, predicting the outputs with a mean absolute error (MAE) of 0.61 MPa and 0.0002, respectively when evaluated on a dedicated unseen test dataset. The models' predictions for the test data set are discussed in Appendix C.

Table 1 Details for artificial neural network (ANN) models

Features	ANN($\bar{\sigma}$)	ANN(α)
Node distribution	16x16x16x16x16x16	48x32x32x48
# tunable parameters	1441	4792

Batch size	8	4
Optimizer	ADAM	ADAM
Activation function	Softplus	Sigmoid
Loss function	MSE	MSE
Metric function	MAE	MAE
Error	0.61 MPa	0.0002

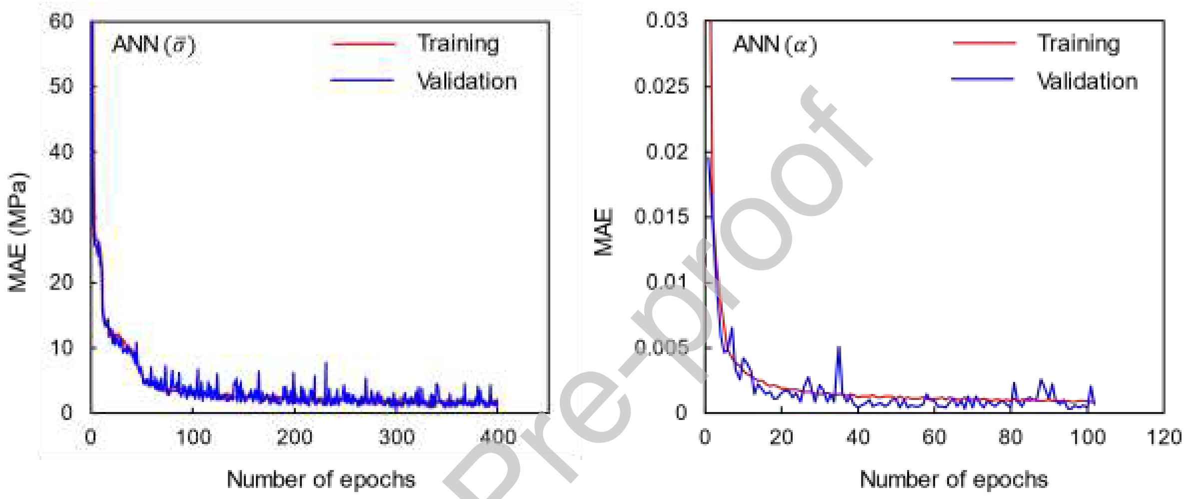

(a) (b)

Figure 10 Learning curves of (a) ANN($\bar{\sigma}$) and (b) ANN(α).

4.3 ANN predictions at intermediate conditions with work hardening comparison

The validity of ANN($\bar{\sigma}$) under untrained temperature and strain rate is assessed by comparing the stress-strain curves tested at an intermediate of training conditions, i.e., T=10˚C and $\dot{\bar{\varepsilon}}$ =0.005 /s. As shown in Figure 11, the ANN($\bar{\sigma}$) prediction closely align with the experimental flow curve, with a maximum mean absolute deviation of less than 4.6 MPa across three repetitions. The accurate prediction of flow curve demonstrates that the developed ANN($\bar{\sigma}$) can capture the strain hardening behavior of CP-Ti well within the training range.

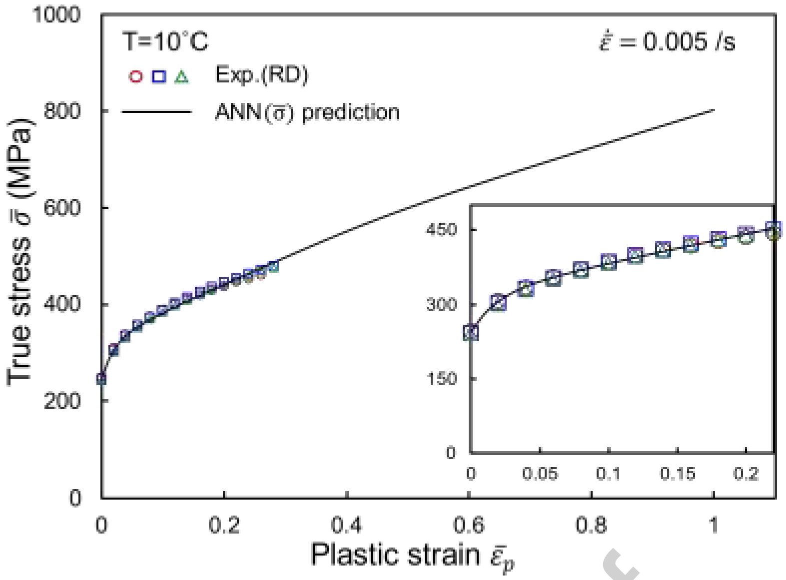

Figure 11 Comparison of experimentally measured and ANN($\bar{\sigma}$) predicted hardening curves at a temperature of 10˚C and strain rate of 0.005 /s. Each symbol indicates an experiment trial.

To further validate the ANN($\bar{\sigma}$) model, the stress strain response in a varying temperature uniaxial tension (UT) test at a constant displacement is investigated. During the test, the temperature varies from -1°C to 20°C and the specimen is loaded at a constant strain rate of 0.0074 /s. The temperature of the test specimen is controlled using a cooling plate attached to its rear as mentioned in Section 1.1, and a uniform temperature of -1°C is obtained on the gage area at the beginning of the test. To vary the temperature of the specimen, the cooling plate is detached from the specimen right before the beginning of the test, ensuring a gradual increase in temperature by exchanging heat with the atmosphere. The variation of temperature and plastic strain during the test is shown in Figure 12a. The experimental data is then fed into the ANN($\bar{\sigma}$) and the predictions are compared in Figure 12b. The good agreement between the ANN($\bar{\sigma}$) prediction and the experimental stress-strain response reaffirms the model's capability to accurately predict complex conditions.

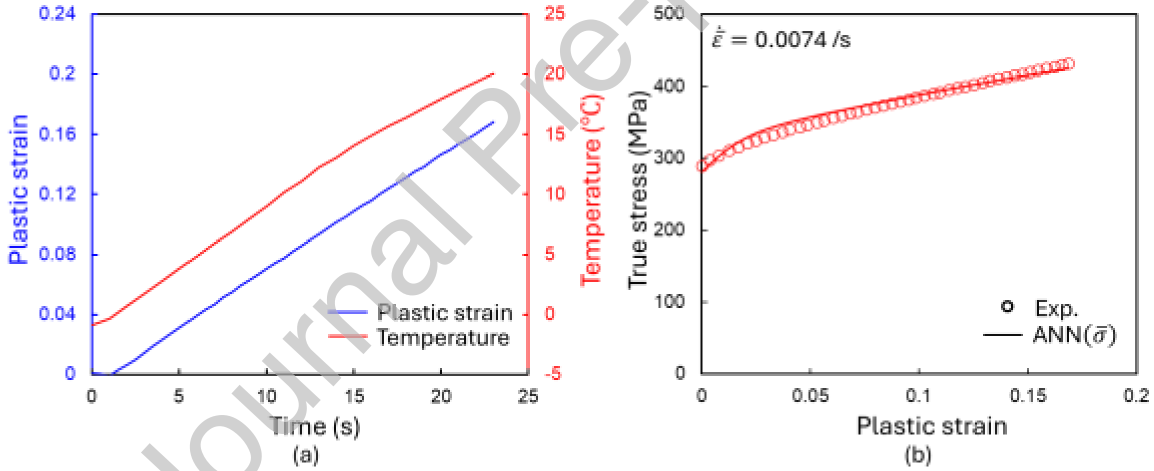

Figure 12 (a) Variation of plastic strain and temperature during the varying temperature UT test and (b) Comparison of ANN($\bar{\sigma}$) prediction with varying temperature UT test results.

Conversely, the validation of ANN(α) is carried out through the ductile fracture tests conducted at the intermediate conditions (see Section 5). For this, the developed ANN models are implemented into user material subroutines (UMAT) for the FE simulations using Abaqus/Implicit. Figures 13a and 13b show the ANN(α) predictions and the corresponding yield loci evolutions with respect to the plastic work at T=10˚C and $\dot{\varepsilon}$ =0.005 /s. The ANN(α) efficiently learns the trends exhibited by each yield function parameter for CP-Ti from the training data and successfully extends this to predict the parameters for the unseen condition. The model predicts the strong differential hardening in the yield loci at small plastic work and the saturation near 45 MJ/m^3 similar to the training conditions.

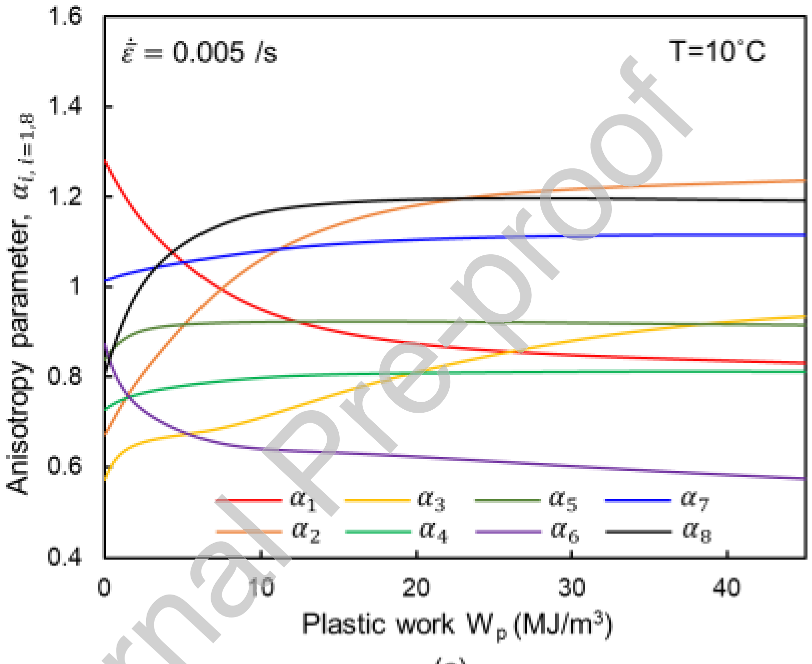

(a)

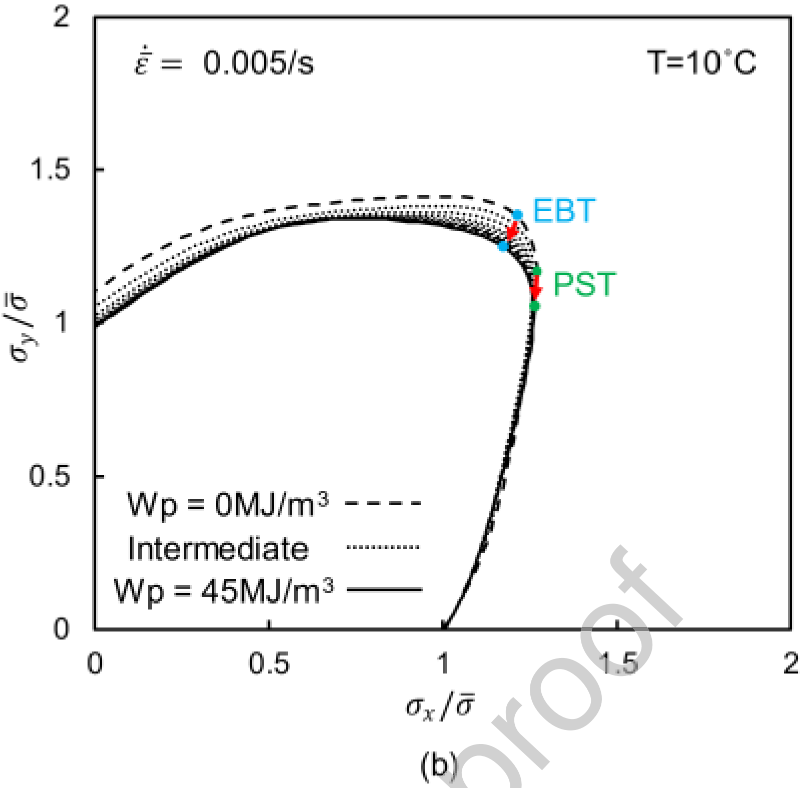

Figure 13 (a) ANN(α) prediction for Yld2000-3d parameters at T=10˚C and $\dot{\bar{\varepsilon}}$=0.005 /s and (b) corresponding yield loci with plastic work W_p.

5. Ductile fracture of CP-Ti

5.1 Ductile fracture models

The developed model capturing plastic behavior of CP-Ti can be used with uncoupled ductile fracture models to investigate ductile fracture behavior across positive stress triaxiality condition ($\eta > 0$). It should be noted that negative stress triaxiality condition ($\eta < 0$) is not considered in the current study because the fracture strain under positive triaxiality is usually much lower than negative range. In this reason, the strength differential effect exiting in CP-Ti is not included in the modelling framework although the importance is fully acknowledged. Among the various models outlined in the Introduction, this work adopts Johnson-Cook (JC), Hosford-Coulomb (HC), and Lou-2014 criteria for ductile fracture analysis of CP-Ti across positive triaxiality.

The stress state of the material is characterized using dimensionless scalars, namely stress triaxiality η and Lode angle parameter $\bar{\theta}$. Stress triaxiality is a representation of the ratio between the first Cauchy and second deviatoric stress tensors invariants. Conversely, the Lode angle parameter $\bar{\theta}$ measures the ratio of the third and second deviatoric stress tensors invariants. These parameters represent the influence of hydrostatic pressure and deviatoric stress on fracture strain, respectively. The formulas defining these parameters are,

$$\eta = \frac{\sigma_m}{\bar{\sigma}} = \frac{I_1}{3\bar{\sigma}} \tag{15}$$

$$\bar{\theta} = 1 - \frac{2}{\pi}\operatorname{acos}\left(\frac{3\sqrt{3}}{2}\frac{J_3}{\sqrt{J_2^3}}\right) \tag{16}$$

where $I_1$is the first Cauchy, and the J_2 and J_3 are the second and third deviatoric stress invariants.

The JC model characterizes the ductile fracture strain $\bar{\varepsilon}_{JC}^f$ as a function of stress triaxiality η, strain rate $\dot{\varepsilon}$, and temperature T. Since the temperature and strain rate effects are neglected in the current ductile fracture study, the expression for the JC model reduces to,

$$\bar{\varepsilon}_{JC}^f = D_1 + D_2 \exp(-D_3\,\eta) \tag{17}$$

where $D_{i,1-3}$ are material constants.

The HC model, proposed by Mohr and Marcadet (2015), transforms the principal stress space into the domain of equivalent plastic strain $\bar{\varepsilon}$, stress triaxiality η, and the Lode angle parameter $\bar{\theta}$ for the fracture prediction. Based on micromechanical considerations, the HC model defines the plastic strain at the onset of fracture $\bar{\varepsilon}_{HC}^f$ as,

$$\bar{\varepsilon}^{f}_{HC}(\eta,\bar{\theta}) = b(1+c)^{\frac{1}{q}}\left[\left\{\left(\frac{(f_1-f_2)^a+(f_2-f_3)^a+(f_1-f_3)^a}{2}\right)\right\}^{\frac{1}{a}} + c(2\eta+f_1+f_3)\right]^{-\frac{1}{q}} \tag{18}$$

with the Lode angle parameter dependent trigonometric functions,

$$f_1[\bar{\theta}] = \frac{2}{3}\cos\left(\frac{\pi}{6}(1-\bar{\theta})\right) \tag{19}$$

$$f_2[\bar{\theta}] = \frac{2}{3}\cos\left(\frac{\pi}{6}(3+\bar{\theta})\right) \tag{20}$$

$$f_3[\bar{\theta}] = -\frac{2}{3}\cos\left(\frac{\pi}{6}(1+\bar{\theta})\right) \tag{21}$$

The Lou-2014 model describes the ductile fracture in a 3D space of stress triaxiality η, Lode parameter L ($\cong -\bar{\theta}$), and equivalent plastic strain $\bar{\varepsilon}^{f}_{Lou}$. The model extends the ductile fracture below a stress triaxiality of $-1/3$ by introducing a cut off function. The model consists of four material parameters C_1, C_2, C_3 and C, in which C determines the cut off value for stress triaxiality. There is no fracture for $\eta < -1/3$, when $C = 0$, while the model predicts the fracture for uniaxial compression, plane strain compression, and equibiaxial compression (where $\eta < -1/3$), when $C = 1/3$.

$$\bar{\varepsilon}^{f}_{Lou}(\eta,L) = C_3\left(\frac{2}{\sqrt{L^2+3}}\right)^{-C_1}\left(\frac{\eta+\frac{3-L}{3\sqrt{L^2+3}}+C}{1+C}\right)^{-C_2} \tag{22}$$

The Lode parameter is expressed as $L = \frac{2\sigma_2 - \sigma_1 - \sigma_3}{\sigma_1 - \sigma_3}$ when σ_1, σ_2, and σ_3 indicate the principal stresses ($\sigma_1 > \sigma_2 > \sigma_3$).

For non-proportional loading conditions, the fracture strain under proportional loading is incorporated into a damage indicator D framework as,

$$D = \int_0^{\bar{\varepsilon}_f} \frac{d\bar{\varepsilon}}{\bar{\varepsilon}_{pr}^{f}(\eta, \bar{\theta})} \tag{23}$$

where $\bar{\varepsilon}_f$ is the accumulated equivalent plastic strain at the onset of fracture along a non-proportional path. The damage indicator D evolves from 0 for undeformed to 1 for the onset of fracture states.

This work primarily focuses on developing a robust modeling approach using artificial neural networks (ANNs) to describe the complex plastic behavior of CP-Ti, which is highly sensitive to temperature and strain rate. The ductile fracture analysis of CP-Ti is discussed as a validation for the proposed approach. Consequently, the temperature and strain dependency of ductile fracture (Li et al., 2023; Pandya et al., 2020) is not considered in this work.

While the Yld2000-3d function is incorporated in this study to account for plastic anisotropy, it is assumed that the fracture response remains isotropic, meaning the initiation of fracture is not influenced by the orientation of the stress tensor relative to the material coordinate system. As this work primarily focus on developing a robust modeling approach using ANNs to describe the complex plastic behavior of CP-Ti, which is sensitive to temperature and strain rate, the ductile fracture analysis of CP-Ti is discussed as a validation for the proposed approach. Hence the temperature and strain rate dependency of the ductile fracture is beyond the scope of this study. The temperature and strain dependency of ductile fracture can be found (Li et al., 2023; Pandya et al., 2020).

5.2 Experiments for ductile fracture characterization

Ductile fracture is characterized along the positive triaxiality range under four loading paths, including uniaxial tension (UT), shear (SH), and biaxial tensions near equibiaxial stretching (BT1) and plane strain tension (BT2) using specimens as illustrated in Figure 14. The central hole specimen, used for uniaxial tension fracture near the hole edge has a 4 mm diameter hole at the center. The outlines of samples are fabricated using abrasive water jet and the holes are made by drilling followed by milling to ensure a high-quality surface to enhance the fracture resistance. For the shear fracture (SH), a notched specimen geometry is determined following the methodology proposed by Roth and Mohr (2018), which takes into account the strain hardening and ductility. To address the uncertainty of ductility prior to testing, three different specimens are tested, and the one with the highest strain is selected for the shear fracture characterization, as shown in Figure 14b.

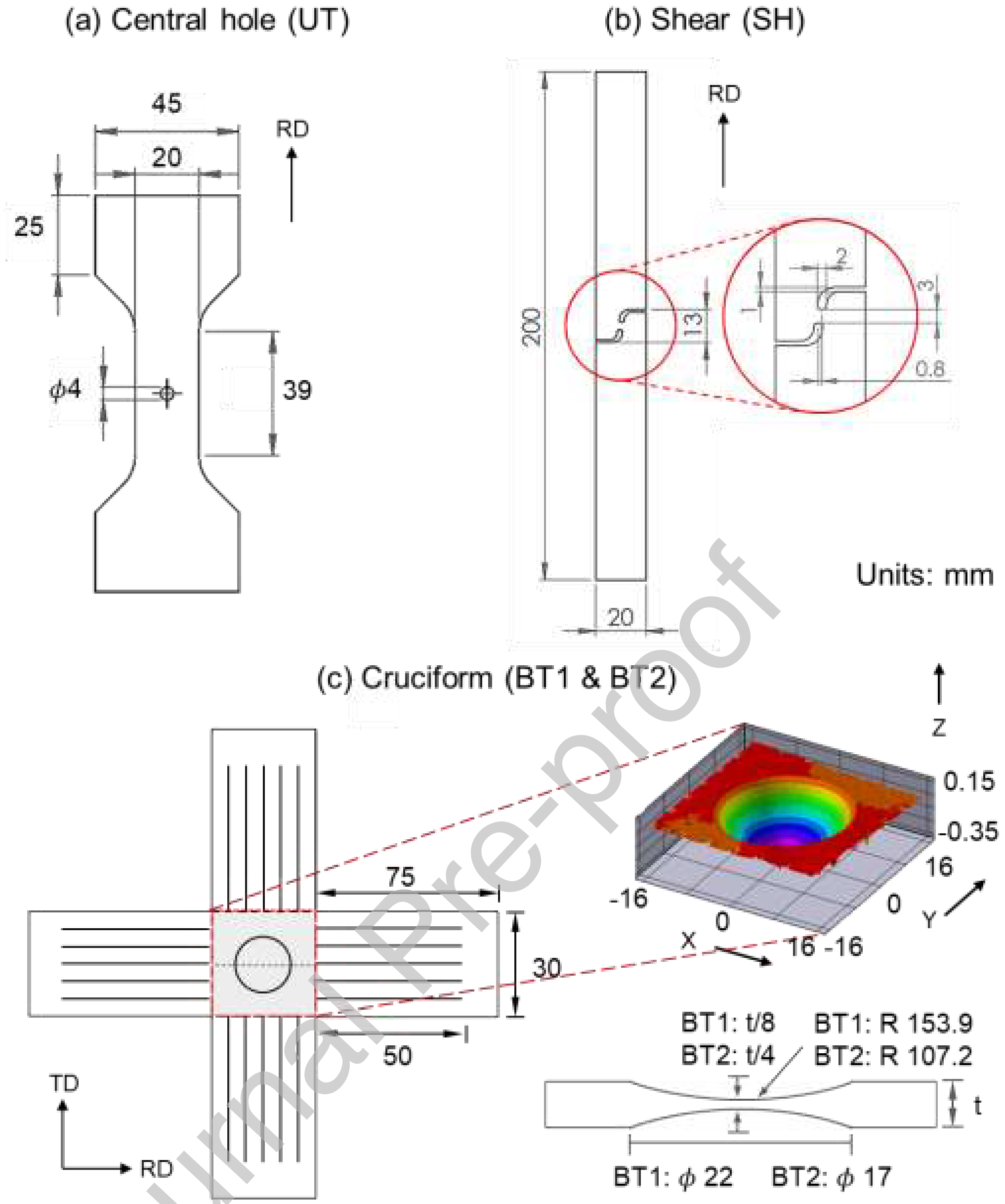

Figure 14 Specimen geometries for ductile fracture characterization: (a) central hole for uniaxial tension (UT), (b) notch for shear (SH), and (c) cruciform with double-sided dimples at the center for biaxial tensions (BT1 and BT2).

For biaxial tensions (BT1 and BT2), the modified cruciform with dimples positioned at the center of both faces introduced by Ha et al. (2019) is used. This design aims to concentrate deformation towards the geometric center of the specimen, resulting in fracture in the center and enabling the fracture strain measurement using the DIC system from the surface. In this study, similar geometries are adopted to probe two biaxial tension stress states, i.e., near equibiaxial (BT1) and plane strain tension

(BT1). The dimples are defined by intersecting a radius R, i.e., 153.9 and 107.2 mm, with the specimen surface and specifying the diameter ϕ of the circles related to the 2D arc length, i.e., ϕ 22 and ϕ 17 mm, for BT1 and BT2, respectively, as depicted in Figure 14c. The cruciform geometries with five slits on each arm are initially fabricated using abrasive water jet cutting, followed by the machining of the dimples using a 3-axis HAAS CNC machine with end-milling. A customized fixture is employed to securely hold and align the specimen during the milling process, ensuring support for the bottom face while the dimples are machined on the opposite face.

The ductile fracture experiments are conducted under unseen temperature and strain rate conditions, i.e., T=10˚C and $\dot{\bar{\varepsilon}}$=0.005 /s. The experiments for UT and SH are performed using the MTS landmark 370 servo-hydraulic universal testing machine, and for BT1 and BT2, the in-plane displacement controlled biaxial loading frame is used (Deng et al., 2015). The displacements ratios $\delta_{RD}:\delta_{TD}=$1:1 and $\delta_{RD}:\delta_{TD}=$ 44:1 are applied to the BT1 and BT2 specimens to achieve near equibiaxial and plane strain tension, respectively. The detailed specifications of these machines along with the temperature control setup and the DIC system are previously provided in Section 2.1 and Section 2.2. From the ductile fracture experiments, the force-displacement ($F-\delta$) and local surface strain ($\varepsilon-\delta$) curves, including the full strain field from the surface, are measured using the testing machine and the DIC systems. The details of local strain and displacement measurements from the specimens are described in Appendix D.

5.3 Validation of plasticity models with hybrid approach

The DIC system effectively captures the local strain field on the surface, but it has limitations in assessing fracture properties due to the inability to directly measure local stress and strain fields inside the material. Therefore, fracture initiation conditions are estimated through FE simulations of the fracture experiments using the developed ANN plasticity models. The simulations are conducted using the commercial software Abaqus/Implicit where the ANN ($\bar{\sigma}$) and ANN (α) are implemented into the UMAT subroutine as shown in the flowchart of Figure 15. General cutting plane method (GCPM) as described in Appendix E is employed as the stress update algorithm (Lee et al., 2022). The neural networks are translated into Fortran code as a subroutine with the weights and biases exported from the Python interface where the ANN models are originally developed.

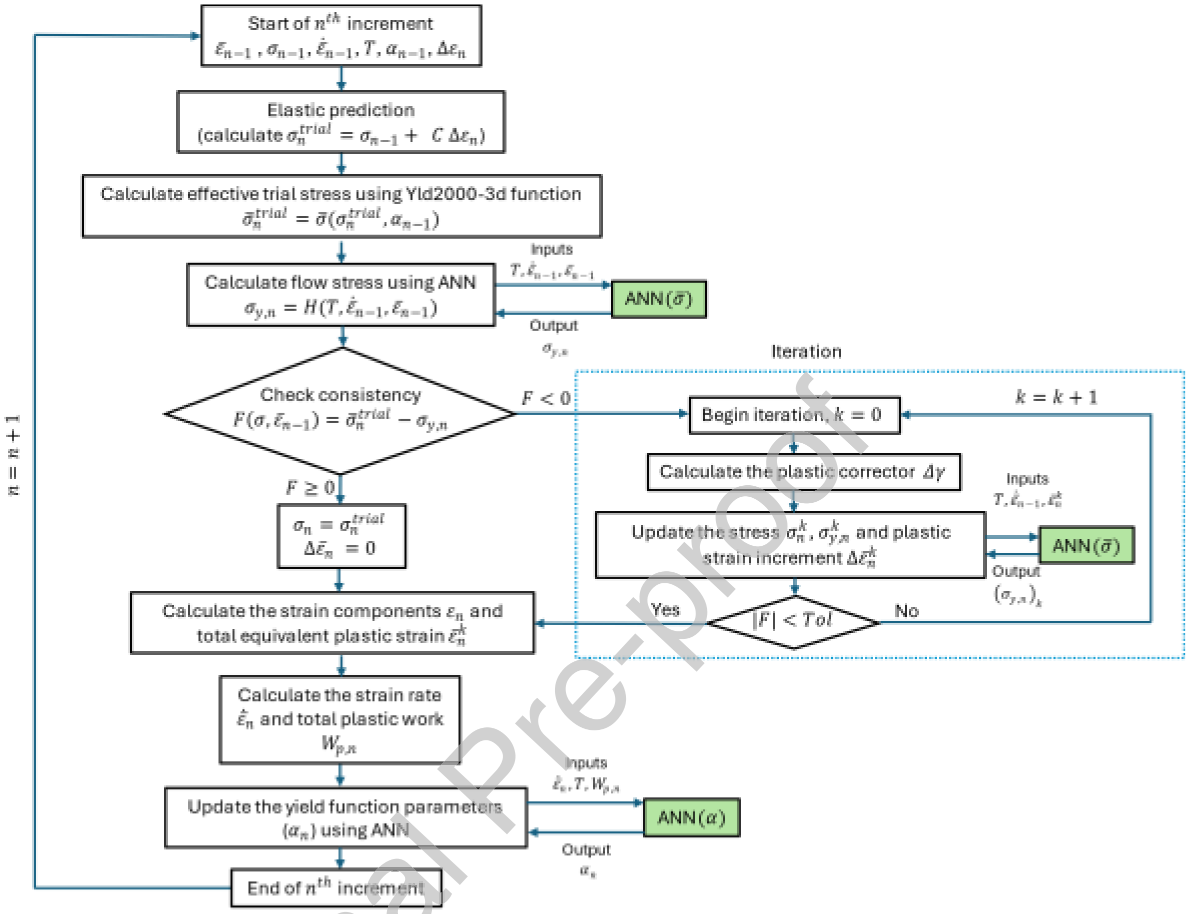

Figure 15 Flow chart showing incorporation of ANN($\bar{\sigma}$) and ANN(α) within the Abaqus/Implicit UMAT subroutine.

Considering the symmetry of the sample geometry about the three mutually perpendicular axes, 1/8 models are created for the FE simulation of UT, BT1, and BT2 specimens, while the asymmetric SH specimen allows only a full model. All models are meshed with 8 node linear brick elements using reduced integration (C3D8R) as shown in Figure 16. To investigate the importance of capturing the differential hardening of CP-Ti on the hybrid experimental-numerical approach, in the present work, two cases of yield function parameters are compared: one with evolving parameters predicted by the ANN model with respect to the plastic work, referred to as ANN(α), and the other with constant parameters at W_p=45 MJ/m³, named as Const.(α), which are often used by researchers.

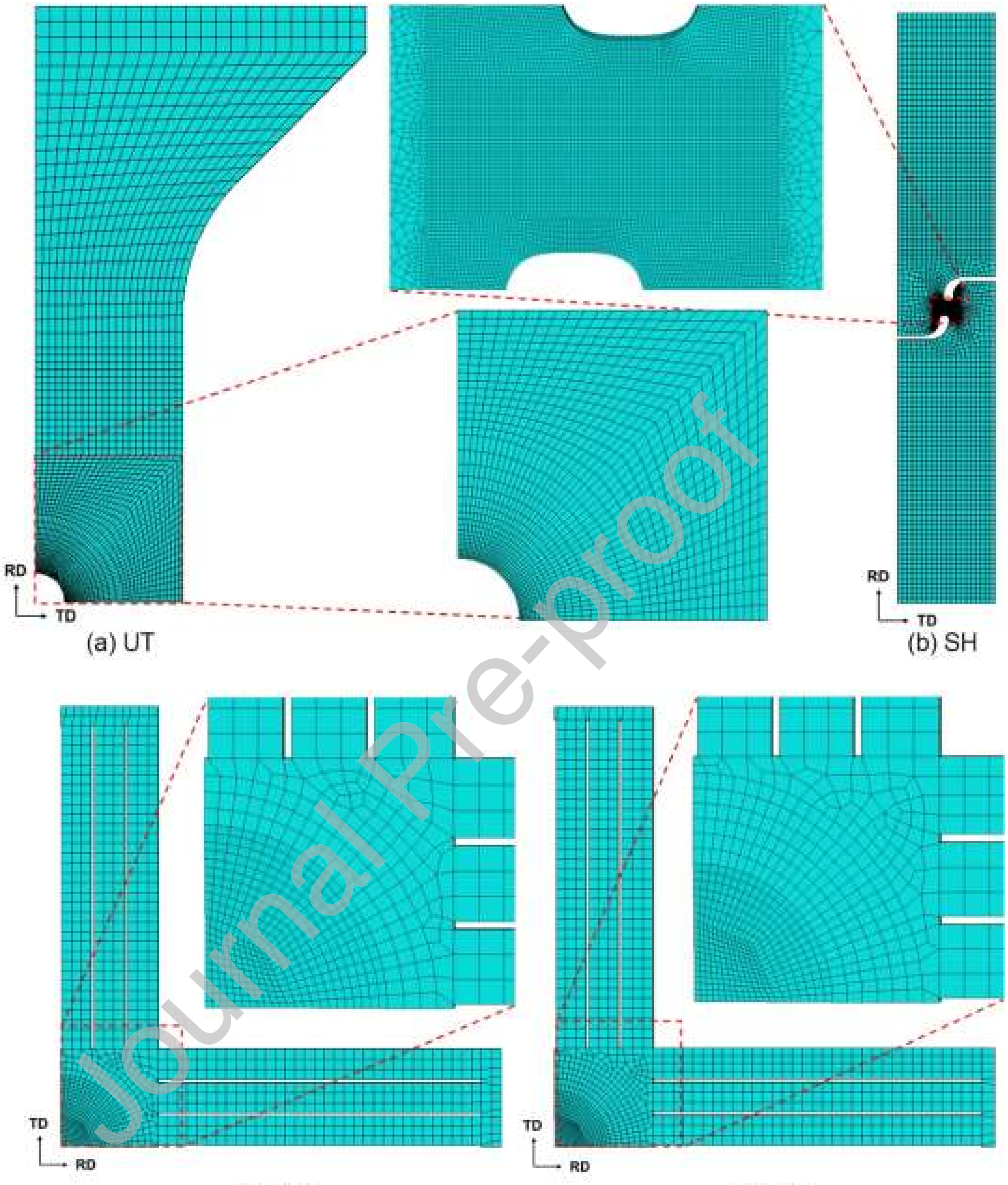

Figure 16 Mesh design for fracture specimens for (a) UT (b) SH, (c) BT1, and (d) BT2.

The experimental force-displacement $(F - \delta)$ and local surface strain-displacement $(\varepsilon - \delta)$ curves are compared to validate the FE model predictions. The comparison of ductile fracture experiments and FE simulations until fracture initiation are illustrated in Figures 17a to 17d. Overall, FE simulations with ANN(α) provide better agreement with the experiments compared to the results with Const.(α), except for BT2, but the difference is minor. Both models overpredict the hardening rate in SH, which indicates that the uniaxial tension experiment in DD using an ASTM E8 specimen (in Section 2.1) is not sufficient to characterize the shear deformation of CP-Ti and requires future improvement, e.g., including additional shear testing for the ANN model training and validation.

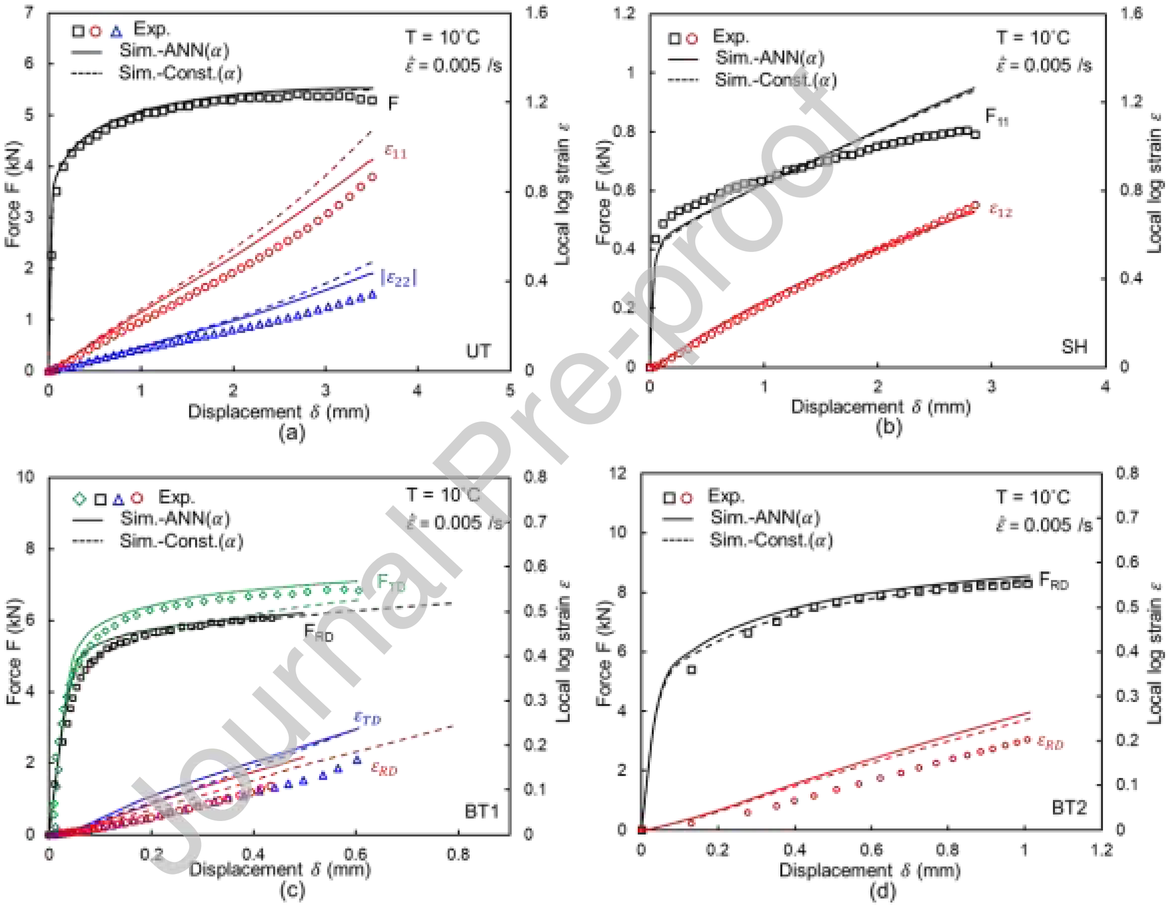

Figure 17 Force-displacement and local strain-displacement curves from experiments and FE simulations for ductile fracture specimens (a) UT, (b) SH, (c) BT1, and (d) BT2.

The $F-\delta$ curve obtained from the UT simulations using both ANN(α) and Const.(α) models closely overlap each other (Figure 17a). The ANN models, especially

ANN($\bar{\sigma}$), prove the capability by providing a reasonably accurate prediction of the material hardening behavior even when trained with limited data, thereby eliminating additional effort for experiments and parameter calibration. For the $\varepsilon - \delta$ curves along the axial and transverse directions, the predictions from ANN(α) lie closer to the experimental curve compared to the predictions from Const.(α). Full strain fields measured by the DIC system at the onset of fracture, i.e., the image prior to a crack being visible, are compared in Figure 18. Local strains are highly concentrated near the hole where the stress state is close to uniaxial tension, but the material can reach a higher strain than an ASTM E8 uniaxial tension test before the fracture. Both ANN(α) and Const.(α) models reasonably well reproduced the experimental strain fields along the axial and transverse directions. However, it should be noted that the local strain of Const.(α) is slightly overpredicted than the ANN(α) and experiment.

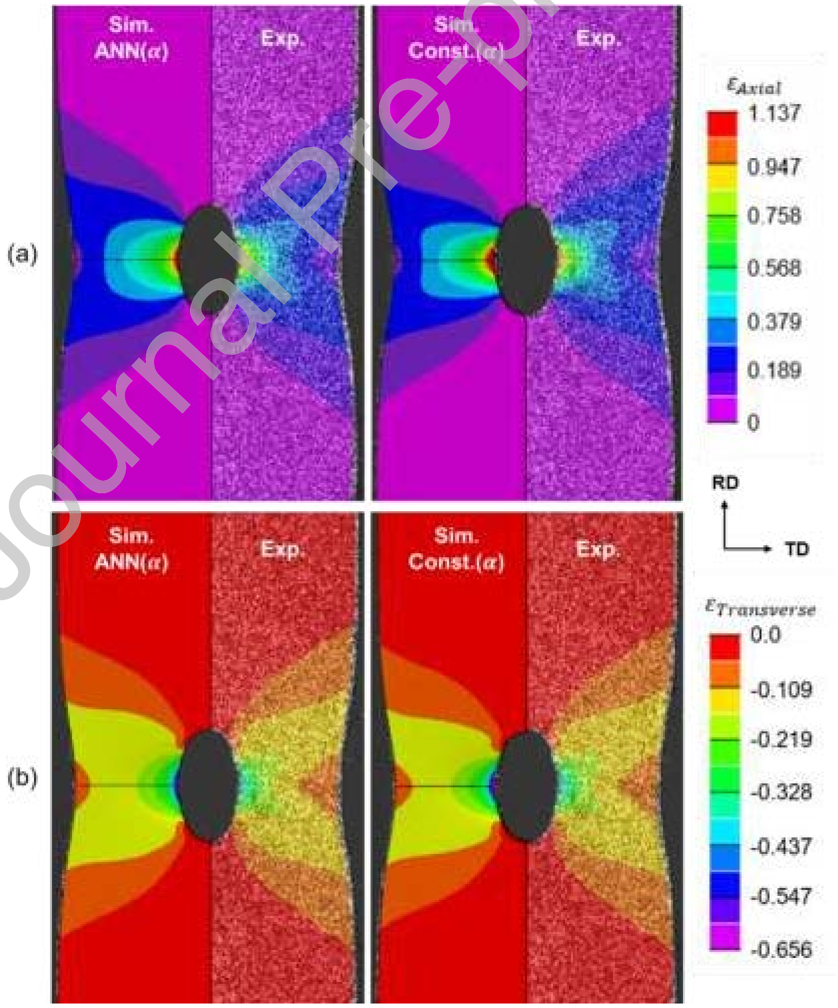

Figure 18 Comparison of surface strain distribution along (a) axial and (b) transverse directions in UT at the onset of fracture obtained from the experiment and FE simulations.

For SH, both models show very close predictions for the $\varepsilon - \delta$ curve in Figure 17b. The strong plastic anisotropy of the CP-Ti as discussed in Section 2.3 and Section 3.2 is one of the key reasons for the inaccuracy in the SH simulations. Yld2000-3d yield function, calibrated by a conventional method using the uniaxial tensions and equibiaxial tension tests, is not flexible enough to capture the shear deformation at the same time. It should be noted that the uniaxial tension in the DD is the only test input including the shear stress component used for the yield function parameter calibration of this work, which leads to overprediction of shear flow stress, i.e., $\sigma_{xy}/\bar{\sigma} = 0.82$ at 45 MJ/m^3. This contributes to the observed deviations between experimental and simulation results using ANN(α) and Const.(α). While the $\varepsilon - \delta$ predictions at the maximum strain localization are in good agreement with the experiment, the full strain field predictions in Figure 19 miss the localization pattern in the experiment, which are caused by the same limitations as the $F - \delta$ curve.

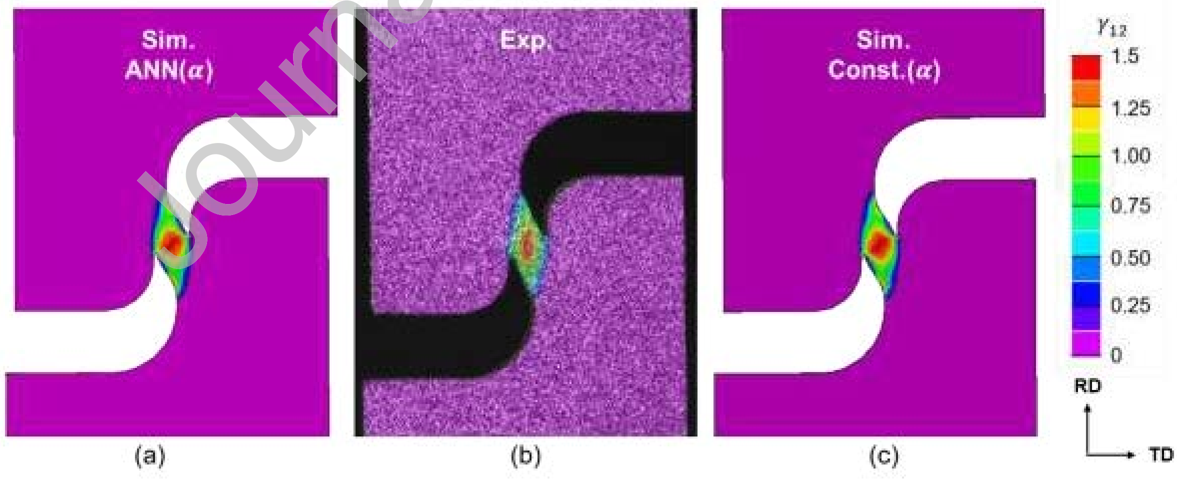

Figure 19 Comparison of shear surface strain distribution in SH at onset of fracture obtained from the experiment and FE simulations.

Under the equibiaxial stretching (BT1), the CP-Ti material clearly exhibits high anisotropy as is evident in the distinct $F - \delta$ and $\varepsilon - \delta$ responses observed in the RD and TD (Figure 17c). The predictions of force and local strain in the RD and TD from the ANN(α) align with the experimental results better than the Const.(α). Const.(α) is closer to the experimental strain along the RD and TD at a specific δ, but it highly overpredicts the displacement to fracture in the RD and underpredicts the transverse force F_{TD}. This can be attributed to the missing prediction of strong differential hardening near equibiaxial and plane strain tension if constant α values are used as illustrated in Figure 13b by the ANN(α). For this reason, the surface strain fields at the onset of fracture (Figure 20) are missed by the Const.(α), while the ANN(α) predicts the distribution of ε_{RD} and ε_{TD} with fair resemblance to the experiment. (The crack propagation is shown in Appendix F.)

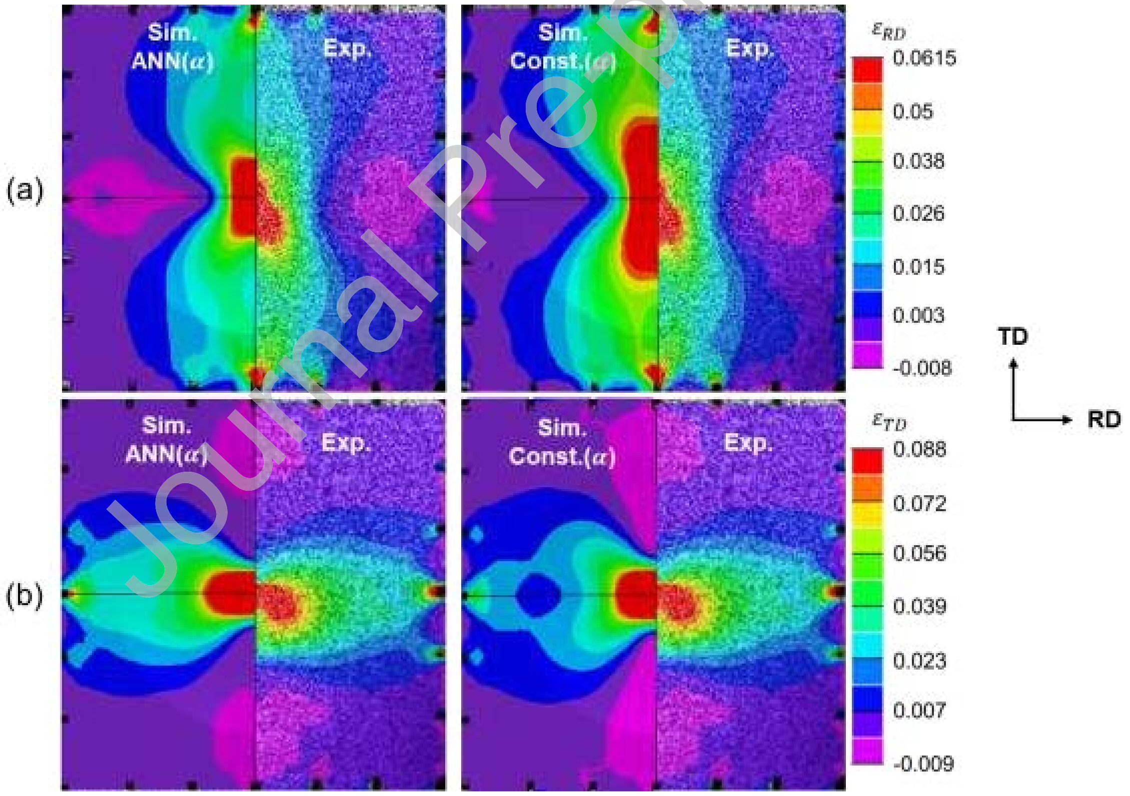

Figure 20 Comparison of surface strain distribution along (a) RD and (b) TD in BT1 at the onset of fracture obtained from the experiment and FE simulations.

For BT2, the strain and displacement along the TD are very small due to the plane strain tension deformation in the center of specimen, and thus Figure 17d presents the force and strain data solely along the RD. Both ANN(α) and Const.(α) models closely replicate the $F_{RD} - \delta_{RD}$ and $\varepsilon_{RD} - \delta_{RD}$ curves, matching well with the experimental values. Since the evolution of the yield locus near the plane strain tension along the RD is negligible (refer Figure 13b), it is expected that the FE models based on both evolving and constant parameters of the yield function yield similar results. However, the ANN(α) strain field prediction shows slightly superior agreement with experimental results. This is evidenced by the similar vertical lengths of severe positive strain (red region at the center) in Figure 21a, and the prediction of severe negative strain (blue regions at top and bottom of the center) in Figure 21b. (The crack propagation and the strain path are shown in Appendix F.)

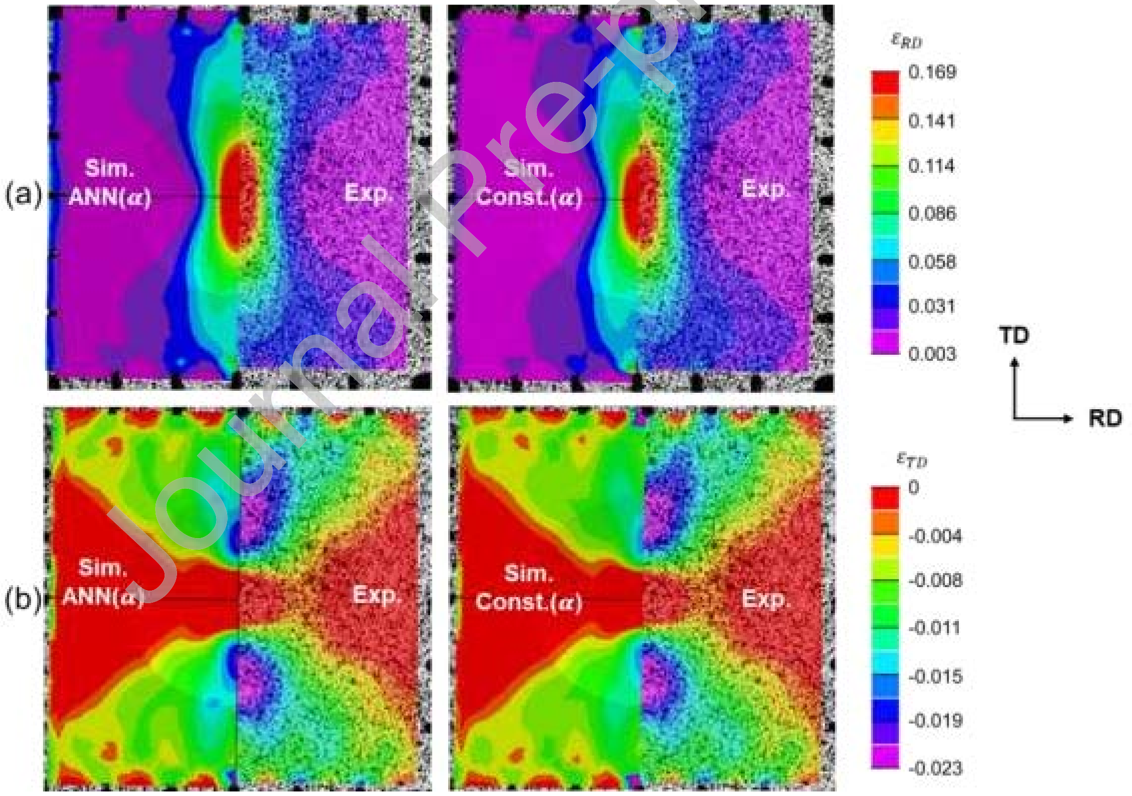

Figure 21 Comparison of surface strain distribution along (a) RD and (b) TD in BT2 at the onset of fracture obtained from the experiment and FE simulations.

Overall, the ductile fracture simulations at unseen conditions show remarkable agreement with the experiments across various stress triaxialities. This highlights the successful integration of ANNs within the phenomenological framework without sacrificing the accuracy or computational stability of FE modeling.

5.4 Construction of ductile fracture envelope for CP-Ti

The hybrid experimental-numerical analysis of ductile fracture of CP-Ti validates the efficiency of ANN(α) in the previous section. The comparison of the experiments and simulations underscores the successful prediction of ANN models at unseen testing conditions, i.e., T=10˚C and $\dot{\varepsilon} = 0.005$ /s. Consequently, the key parameters necessary for fracture model calibration, such as fracture strain $\bar{\varepsilon}_f$, stress triaxiality η, and Lode angle parameter $\bar{\theta}$ (or Lode parameter L), are extracted from the simulations with the ANN(α). These parameters are extracted from critical locations within the ductile fracture specimens where fracture is initiated. For instance, the data is extracted at the center of dimple for BT1 and BT2, at the edge of central hole for UT, and at the middle of narrow gage section for SH. Assuming the fracture is initiated at the location of highest equivalent strain, equivalently where the deformation is mostly concentrated, all extraction points are consistently positioned at the midplane through the specimen thickness.

The loading paths to fracture are crucial for ductile fracture model calibration, as they capture the loading history of the critical point of the material from the beginning of loading until the fracture is initiated. The loading paths from the four ductile fracture specimens are plotted in relation to stress triaxiality η and Lode angle parameter $\bar{\theta}$ as depicted in Figure 22. Among the specimens, the UT displays the highest fracture strain $\bar{\varepsilon}_f$ while the lowest is obtained from BT2, i.e., plane strain. With the exception of initial fluctuations, the stress triaxiality η and Lode angle parameter $\bar{\theta}$ remained relatively consistent for UT, BT1, and BT2, indicating the proportional loading subjected in the experiment. It should be noted that stress triaxiality η for plane strain tension and equibiaxial tension are predicted as 0.74 and 0.81, respectively, because of the strong anisotropy in CP-Ti. (The values are 0.58 and 0.67 for the von Mises prediction, respectively). On the other hand, the selected SH specimen shows non-linearities in the loading history with varying stress triaxiality η and Lode angle parameter $\bar{\theta}$. The effect of non-linearity is compensated by the damage indicator in Eq. (23) in Section 5.1 to calibrate the parameters of ductile fracture models.

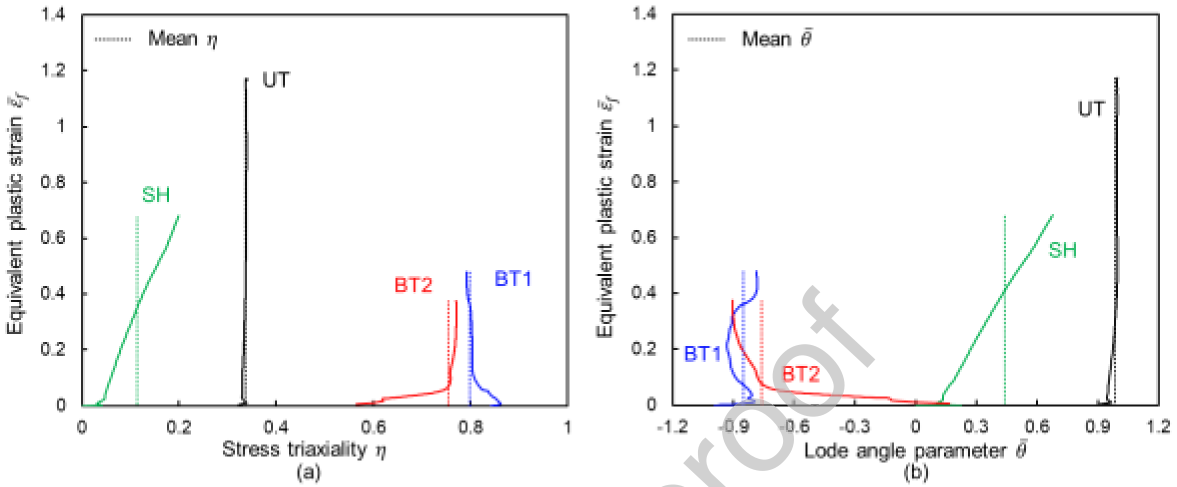

Figure 22 Loading paths to fracture $\bar{\varepsilon}_f$ with respect to (a) stress triaxiality η and (b) Lode angle parameter $\bar{\theta}$.

The optimized parameters for the ductile fracture models are detailed in Table 2. The JC and Lou-2014 models are calibrated through the least square method, while a simplex error minimization algorithm is employed for optimizing the HC model parameters. In the case of the HC model, the parameter q is typically set at 0.1 for most metals. For the Lou-2014 model, the parameter C is set to 0, given our interest lies on $\eta > -0.33$. Figure 23 illustrates the fracture envelopes constructed using HC, Lou-2014, and JC models in the 3D space of $\bar{\varepsilon}_f$, η, and $\bar{\theta}$. The data points for UT, SH, BT1, and BT2 align precisely on the HC and Lou-2014 fracture surfaces. On the other hand, JC model, which is independent of Lode angle parameter produces a fairly flat envelop which fails to capture the failure strain for SH. The asymmetric shapes of fracture envelopes if HC and Lou-2014 underscores the significance of the effect of $\bar{\theta}$ on $\bar{\varepsilon}_f$.

Table 2 Ductile fracture model parameters

HC	$a = 0.846$	$b = 1.362$	$c = 0.189$	$q = 0.1$
Lou-2014	$C_1 = 12.977$	$C_2 = 3.459$	$C_3 = 1.269$	$C = 0$
JC	$D_1 = 0.303$	$D_2 = 0.638$	$D_3 = 2.1$	

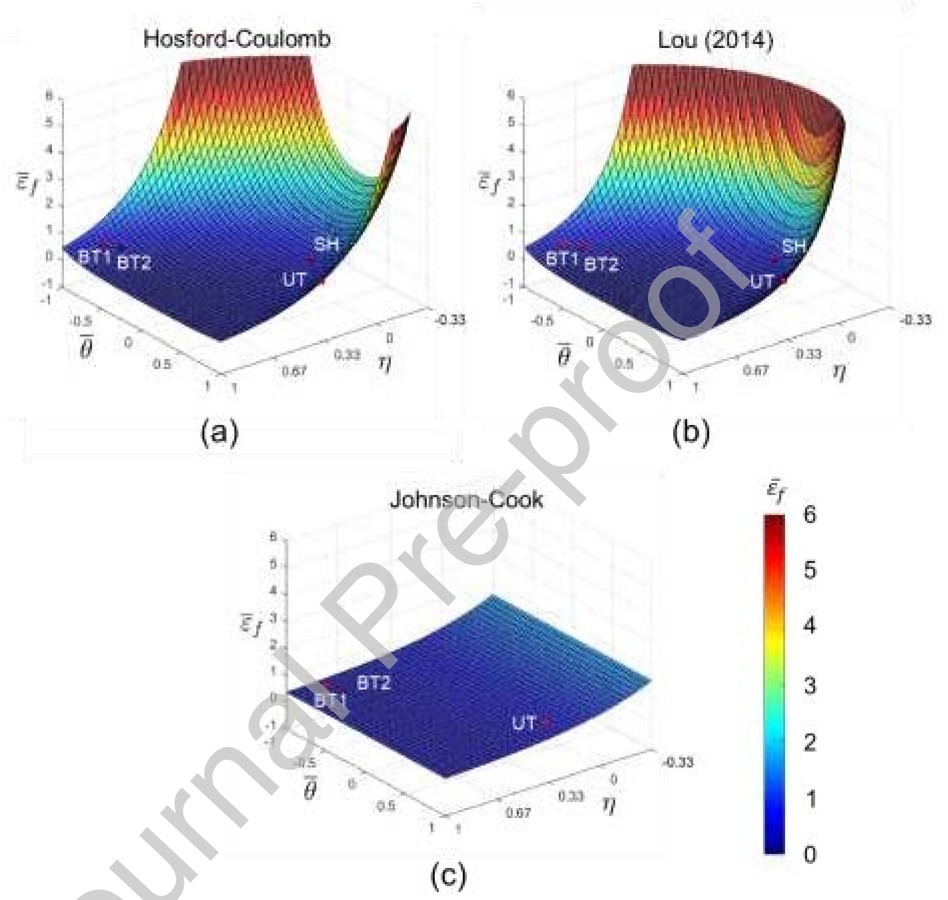

(a) (b) (c)

Figure 23 Fracture envelopes predicted by (a) HC and (b) Lou-2014, and (c) JC models.

6. Conclusions

In this study, a robust modeling approach is proposed by incorporating a machine learning algorithm into an existing anisotropic yield function to describe the complicated temperature and strain rate dependent anisotropic plasticity behavior of CP-Ti. The plasticity of the material is characterized by uniaxial tension tests along the three orientations and the in-plane biaxial tension tests at temperatures of 20°C and 0°C with strain rates of 0.001 /s and 0.01 /s. The results show substantial anisotropy in stresses and strains as evidenced by the distinct stress-strain curves and r-values obtained in different orientations. The material also exhibits a differential hardening behavior with distorted yield loci, which eventually saturates with increased plastic deformation. Two ANNs, i.e., ANN($\bar{\sigma}$) and ANN(α) are proposed to comprehensively describe the plastic behavior of CP-Ti by accounting for factors such as temperature, strain rate, and plastic deformation. The ANN($\bar{\sigma}$) model is used to capture the strain hardening behavior, while the ANN(α) model predicts the anisotropy parameters of the Yld2000-3d yield function. A remarkable alignment is observed between the experiment and prediction for the target conditions at T=10˚C and $\dot{\varepsilon}=$0.005 /s, which distinctly underscores the competency of the ANN models in accurately capturing the temperature and strain rate dependent plastic behavior of the material.

Next, the ductile fracture of the CP-Ti is investigated through a hybrid experimental-numerical analysis by integrating the ANN models with the uncoupled fracture models. This also provide a validation for the proposed ANN models at an unseen temperature and strain rate condition. The fracture behavior is studied under various stress states in positive stress triaxiality range including uniaxial tension, shear, near equibiaxial tension, and plane strain tension at unseen conditions for the ANNs, i.e., T=10˚C and $\dot{\varepsilon}=$0.005 /s. To assess the influence of differential hardening in the hybrid approach of ductile fracture modeling, two cases for Yld2000-3d yield function parameters, i.e., ANN(α) for evolution and Const.(α) for constant values, are employed in the FE simulations. Owing to the substantial differential hardening characteristics of CP-Ti, it is noteworthy that only the ANN(α) could achieve a satisfactory agreement with the experiments consistently across all the tests. This demonstrates the significance of differential hardening on the ductile fracture behavior of CP-Ti and confirms the efficiency of ANN(α) in capturing the anisotropic plastic behavior of the material. The ductile fracture simulations also highlight the computational stability of the developed ANN models while incorporated in FE simulations.

Based on the successful validation of plasticity, the stress triaxiality η, Lode angle parameter $\bar{\theta}$ (or Lode parameter L), and equivalent plastic strain to fracture $\bar{\varepsilon}_f$ are extracted from the FE simulations using ANN(α). While the stress triaxiality η and Lode angle parameter $\bar{\theta}$ of the UT, BT1, and BT2 remain relatively consistent during loading, those of the SH sample are observed to evolve throughout the loading process. Notably, the UT demonstrates the highest fracture strain while the BT2 experiences the fracture at the lowest equivalent plastic strain level. The higher the stress triaxiality η predictions in the BT1 and BT2 compared to the von Mises values can be attributed to the pronounced anisotropic behavior of CP-Ti. Finally, the fracture envelops of CP-Ti are constructed using three ductile fracture models, HC, Lou-2014, and JC.

In conclusion, this research demonstrates the potential of machine learning in unraveling the influence of strain rate and temperature in the anisotropic plastic deformation of CP-Ti. Particularly, the developed ANN models is implemented within the plasticity theory framework excel in capturing the anisotropic, differential hardening, and flow behavior sensitive to temperature and strain rate. Compared to purely data-driven approaches that rely solely on machine learning algorithms, this hybrid approach can leverage the robustness of machine learning while adhering to conventional constitutive equations, providing a balanced and reliable modeling strategy. The similar approach can be incorporated with any constitutive models chosen depending on the material characteristics and applications of interest and still maintain the computational stability in FE simulations. The ANN models used in this study still hold potential for further enhancement by incorporating additional strain rate and temperature conditions for training.

Acknowledgements

This work was funded by the National Science Foundation (NSF) EPSCoR award (#1757371), the New Hampshire Center for Multiscale Modeling and Manufacturing of Biomaterials (NH BioMade). The authors would like to thank Scott Campbell (Senior machinist, College of Engineering and Physical Sciences, UNH) and Nathan Daigle (Manufacturing engineer, John Olson Advanced Manufacturing Center, UNH) for their assistance with fixture design and sample fabrication for the experiments.

Declaration of Generative AI and AI-assisted technologies in the writing process

During the preparation of this work, the author(s) used ChatGPT 3.5 in order to enhance readability, rephrase certain sections, and perform grammar checking. After using this tool/service, the author(s) reviewed and edited the content as needed and take(s) full responsibility for the content of the publication.

Appendix A. Extrapolation of strain hardening behavior

Table A1 Swift-Voce Hardening parameters

Strain rate (/s)	Temp. (˚C)	w_{sv}	Swift			Voce		
			s_0 (MPa)	s_1	s_2	v_0 (MPa)	v_1 (MPa)	v_2
0.001	-10	0.183	33648	0.002	0.003	33059	40136	0.020
	0	1.108	859	0.002	0.469	435	2292	6.106
	20	1.259	613	0.002	0.357	176	656	10.09
0.01	-10	0.057	35167	0.002	0.008	18785	20499	0.036
	0	0.255	19269	0.002	0.005	16273	22290	0.030
	20	1.428	617	0.002	0.407	142	545	6.864

Appendix B. Anisotropic yield loci in (σ_x-σ_y) stress space

Following the experimental characterization of CP-Ti at temperatures of 0°C and 20°C, and strain rates of 0.001 /s and 0.01 /s, the yield loci of CP-Ti are constructed using the Yld2000-3d anisotropic yield function. The yield loci differentially expand with the plastic work, due to strong anisotropy evolution. When plotted in the (σ_x-σ_y) stress space (see Figure B1), the yield loci reveal their actual size, with larger yield loci observed at lower temperatures. This observation is consistent with the results of uniaxial tension tests discussed in Section 2.3.

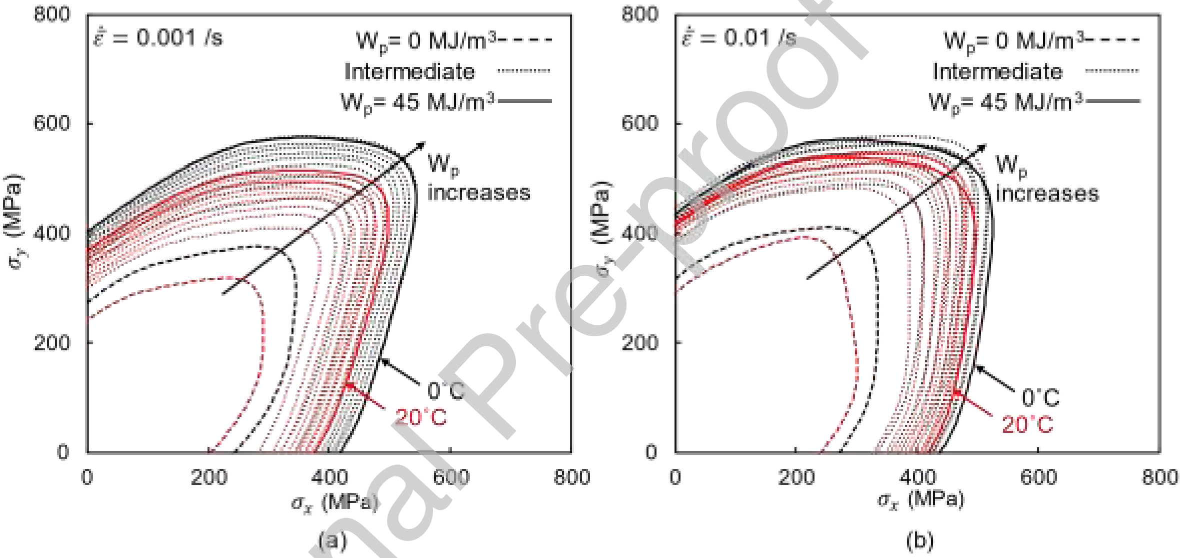

Figure B1 Yield loci of CP-Ti plotted in (σ_x-σ_y) stress space for (a) 0.01/s and (b) 0.001/s strain rates with 0°C and 20°C temperatures.

Appendix C. Performance of ANN models

Fifteen percent of the dataset created for training is set aside to test the performance of the ANN models with unseen data, after training. The ANN($\bar{\sigma}$) and ANN(α) predict outputs with MAE of 0.61 MPa and 0.0002, respectively. The predictions of ANN models are plotted against the corresponding targets as shown in Figure C1. Only 50 random data points from the test data are used for the following figure.

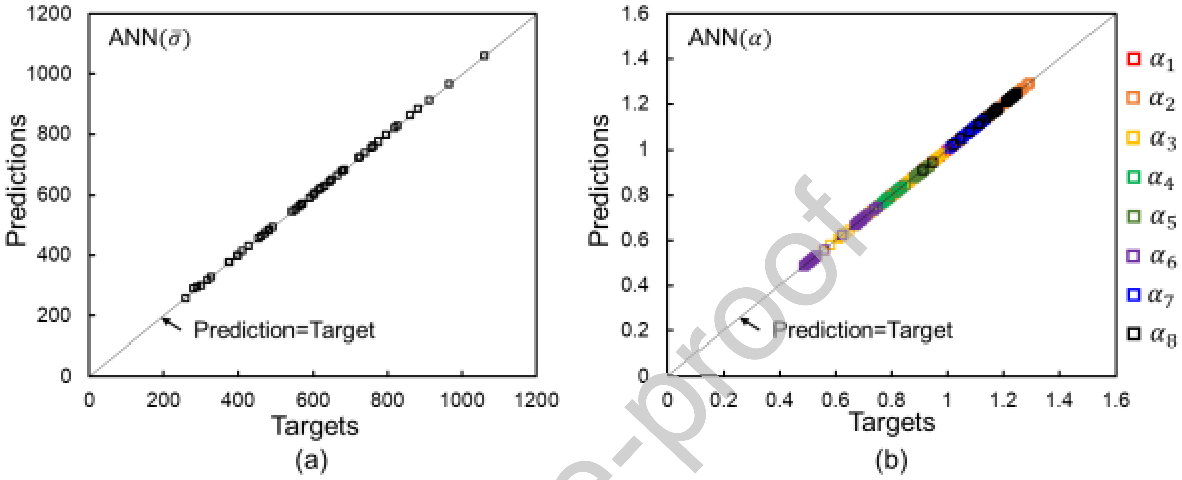

Figure C1 Comparison of predictions and corresponding targets for (a) ANN($\bar{\sigma}$) and (b) ANN(α).

Appendix D. Temperature field and strain measurement

The local strains are extracted at different locations for each ductile fracture specimen as marked in Figure D1. In the UT, the local strains along the axial and transverse directions are obtained at a point 0.4 mm away from the central hole (Figure D1a). In both SH and cruciform specimens for BT1 and BT2, the local strains are extracted from the center of the gauge (Figures D1b – D1d). The displacements δ are obtained using one or two virtual extensometers with an initial length of 20 mm except BT2, where the displacement is determined using a shorter virtual extensometer of initial length 15 mm. The color fields represent how well the temperature distribution is maintained around 10^{o}C until the onset of fracture.

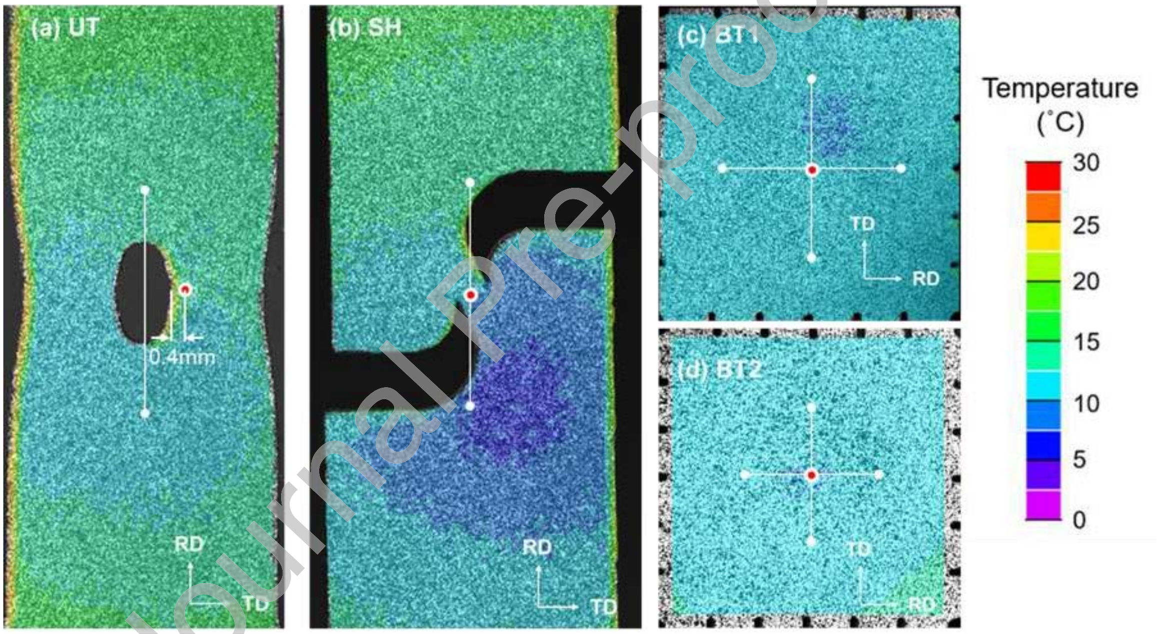

Figure D1 Temperature distribution on ductile fracture specimens captured with IR camera prior to onset of fracture in (a) UT, (b) SH, (c) BT1, and (d) BT2 experiments. The white straight lines are the virtual extensometers used in stereo-DIC, and the red circles indicate the locations where the local strains are extracted from the surface.

Appendix E. Stress update algorithm: general cutting plane method (GCPM)

The general cutting-plane method (GCPM) updates the Cauchy stress $\boldsymbol{\sigma}$ and the relevant state variables at the current time step t_n for a given strain increment $\Delta\boldsymbol{\varepsilon}_n$ (Lee et al., 2022). This algorithm employs Newton–Raphson iteration method (Ortiz and Simo, 1986), initiating with the calculation of elastic predictor.

Assuming the strain increment $\Delta\boldsymbol{\varepsilon}_n$ is entirely elastic, the elastic predictor $\boldsymbol{\sigma}_n^{trial}$ is calculated as:

$$\boldsymbol{\sigma}_n^{trial} = \boldsymbol{\sigma}_{n-1} + \boldsymbol{C} : \Delta\boldsymbol{\varepsilon}_n \tag{E1}$$

where $\boldsymbol{\sigma}_{n-1}$ represents the Cauchy stress at the previous time step t_{n-1}, $\boldsymbol{C}$ is the fourth-order isotropic elasticity stiffness tensor, and ":" denotes a tensor product between the fourth-order and second-order tensors.

If the following condition holds, the trial stress is purely elastic:

$$F_n\left(\boldsymbol{\sigma}_n^{trial}, \bar{\varepsilon}_{n-1}\right) = \phi_n\left(\boldsymbol{\sigma}_n^{trial}\right) - H(\bar{\varepsilon}_{n-1}) \leq 0 \tag{E2}$$

Here, F defines the plastic yielding of the material, while H is the flow stress from the strain hardening model given by ANN$(\bar{\sigma})$ and ϕ is the equivalent stress from the Yld2000-3d yield function as in Eq. (5). When this consistency condition is satisfied, the updated stress $\boldsymbol{\sigma}_n$ at the current step equals the trial stress $\boldsymbol{\sigma}_n^{trial}$, and the equivalent strain and other state variables of the yield function remain as the converged values from the previous time step. If not, i.e., when $F_n(\boldsymbol{\sigma}_n^{trial}, \bar{\varepsilon}_{n-1}) > 0$, the equation is iteratively solved to determine the plastic multiplier $\Delta\gamma$ through return mapping algorithm to ensure the consistency is satisfied. Applying the associated flow rule and Euler's theorem, the relationship between the equivalent plastic strain increment $\Delta\bar{\varepsilon}$ and plastic multiplier $\Delta\gamma$ is obtained as:

$$F_n = \phi(\boldsymbol{\sigma}_{n-1} + \Delta\boldsymbol{\sigma}_n) - H(\bar{\varepsilon}_{n-1} + \Delta\gamma) = \phi(\boldsymbol{\sigma}_n) - H(\bar{\varepsilon}_{n-1} + \Delta\bar{\varepsilon}_n) < tol \tag{E3}$$

$$\Delta\boldsymbol{\varepsilon}^{p} = \Delta\gamma \frac{\partial\phi}{\partial\boldsymbol{\sigma}} \tag{E4}$$

$$\Delta\bar{\varepsilon} = \frac{\boldsymbol{\sigma}\Delta\boldsymbol{\varepsilon}}{\phi(\boldsymbol{\sigma})} = \frac{\boldsymbol{\sigma}\Delta\gamma\frac{\partial\phi}{\partial\boldsymbol{\sigma}}}{\phi(\boldsymbol{\sigma})} = \Delta\gamma\frac{\phi(\boldsymbol{\sigma})}{\phi(\boldsymbol{\sigma})} = \Delta\gamma \tag{E5}$$

where $\Delta\boldsymbol{\varepsilon}$ is the plastic strain tensor increment.

By applying Taylor's expansion to Eq. (E3), the variation of the equivalent plastic strain increment at the k^{th} iteration is:

$$\Delta\bar{\varepsilon}_n^{(k)} = \Delta\bar{\varepsilon}_n^{(k-1)} + \delta(\Delta\bar{\varepsilon}) \tag{E6}$$

and

$$F_n(\Delta\bar{\varepsilon}_n) + \frac{\partial F_n(\Delta\bar{\varepsilon}_n^{k-1})}{\partial\Delta\bar{\varepsilon}}\,\delta(\Delta\bar{\varepsilon}) = 0 \tag{E7}$$

Then,

$$\begin{aligned}\delta(\Delta\gamma) = \delta(\Delta\bar{\varepsilon}) &= {-F_{n+1}\left(\Delta\bar{\varepsilon}_n^{(k-1)}\right)} \Bigg/ {\frac{\partial F_n\left(\Delta\bar{\varepsilon}_n^{(k-1)}\right)}{\partial\Delta\bar{\varepsilon}}} \\ &= \frac{F_{n+1}\left(\Delta\bar{\varepsilon}_n^{(k-1)}\right)}{\frac{\partial\phi_n^{(k-1)}}{\partial\boldsymbol{\sigma}_n^{(k-1)}} : \boldsymbol{C} : \frac{\partial\phi_n^{(k-1)}}{\partial\boldsymbol{\sigma}_n^{(k-1)}} + H'(\Delta\bar{\varepsilon}_n^{(k-1)})}\end{aligned} \tag{E8}$$

where H' is the slope of the strain hardening curve. Finally, the updated stress and equivalent plastic strain are computed as:

$$\boldsymbol{\sigma}_n^{(k)} = \boldsymbol{\sigma}_n^{(k-1)} + \delta(\Delta\bar{\varepsilon})\,\boldsymbol{C} : \frac{\partial \phi_n^{(k-1)}}{\partial \boldsymbol{\sigma}_n^{(k-1)}} \qquad \text{(E9)}$$

and

$$\bar{\varepsilon}_n^{(k)} = \bar{\varepsilon}_n^{(k-1)} + \Delta\bar{\varepsilon}_n^{(k)} \qquad \text{(E10)}$$

Appendix F. Crack propagation and strain field in the cruciform specimens

The ductile fracture specimens are subjected to deformation until any visible cracks are observed through the DIC cameras. In the dimple cruciform specimens, a surface crack becomes evident at the center of the dimple and gradually propagates, leading to the complete opening-up of the specimen at the dimple region. The cracks are formed on the BT1 and BT2 samples along the major principal strain direction as shown in Figure F1: the BT1 sample for equibiaxial stretching exhibits a diagonally oriented crack while the BT2 specimen for plane strain tension (see the strain path in Figure F2) present a crack perpendicular to the major loading axis in the RD.

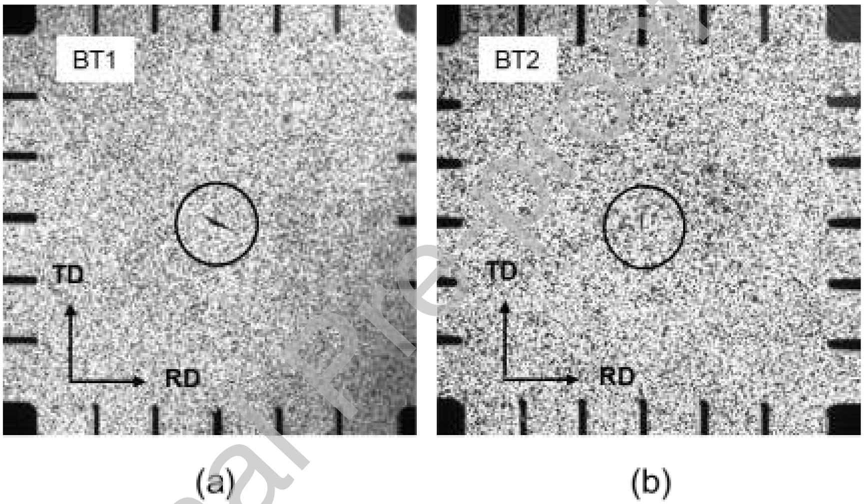

Figure F1 Crack formed on cruciform specimen surface in (a) BT1 and (b) BT2.

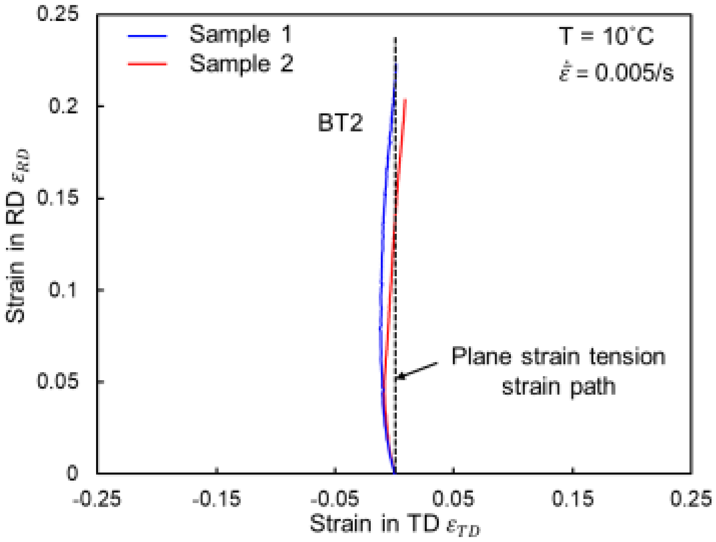

Figure F2 Strain path of BT2 from DIC surface strain measurements.

References

Bai, Y., Wierzbicki, T., 2010. Application of extended Mohr–Coulomb criterion to ductile fracture. Int J Fract 161, 1–20. https://doi.org/10.1007/s10704-009-9422-8

Bai, Y., Wierzbicki, T., 2008. A new model of metal plasticity and fracture with pressure and Lode dependence. International Journal of Plasticity 24, 1071–1096. https://doi.org/10.1016/j.ijplas.2007.09.004

Banabic, D., 2010. Sheet Metal Forming Processes. Springer, Berlin, Heidelberg. https://doi.org/10.1007/978-3-540-88113-1

Bao, Y., Wierzbicki, T., 2004a. A Comparative Study on Various Ductile Crack Formation Criteria. Journal of Engineering Materials and Technology 126, 314–324. https://doi.org/10.1115/1.1755244

Bao, Y., Wierzbicki, T., 2004b. On fracture locus in the equivalent strain and stress triaxiality space. International Journal of Mechanical Sciences 46, 81–98. https://doi.org/10.1016/j.ijmecsci.2004.02.006

Baral, M., Ha, J., Korkolis, Y.P., 2019. Plasticity and ductile fracture modeling of an Al–Si–Mg die-cast alloy. Int J Fract 216, 101–121. https://doi.org/10.1007/s10704-019-00345-1

Baral, M., Hama, T., Knudsen, E., Korkolis, Y.P., 2018. Plastic deformation of commercially-pure titanium: experiments and modeling. International Journal of Plasticity 105, 164–194. https://doi.org/10.1016/j.ijplas.2018.02.009

Baral, M., Ripley, P.W., Lou, Y., Korkolis, Y.P., 2024. Anisotropic ductile fracture of a stainless steel under biaxial loading: Experiments and predictions. International Journal of Plasticity 175, 103927. https://doi.org/10.1016/j.ijplas.2024.103927

Barlat, F., Aretz, H., Yoon, J.W., Karabin, M.E., Brem, J.C., Dick, R.E., 2005. Linear transfomation-based anisotropic yield functions. International Journal of Plasticity 21, 1009–1039. https://doi.org/10.1016/j.ijplas.2004.06.004

Barlat, F., Brem, J.C., Yoon, J.W., Chung, K., Dick, R.E., Lege, D.J., Pourboghrat, F., Choi, S.-H., Chu, E., 2003. Plane stress yield function for aluminum alloy sheets—part 1: theory. International Journal of Plasticity 19, 1297–1319. https://doi.org/10.1016/S0749-6419(02)00019-0

Battaini, M., Pereloma, E.V., Davies, C.H.J., 2007. Orientation Effect on Mechanical Properties of Commercially Pure Titanium at Room Temperature. Metall Mater Trans A 38, 276–285. https://doi.org/10.1007/s11661-006-9040-2

Beese, A.M., Luo, M., Li, Y., Bai, Y., Wierzbicki, T., 2010. Partially coupled anisotropic fracture model for aluminum sheets. Engineering Fracture Mechanics 77, 1128–1152. https://doi.org/10.1016/j.engfracmech.2010.02.024

Benzerga, A., Besson, J., Batisse, R., Pineau, A., 2001. Synergistic effects of plastic anisotropy and void coalescence on fracture mode in plane strain. Modelling and Simulation in Materials Science and Engineering 10, 73. https://doi.org/10.1088/0965-0393/10/1/306

Benzerga, A.A., Besson, J., 2001. Plastic potentials for anisotropic porous solids. European Journal of Mechanics - A/Solids 20, 397–434. https://doi.org/10.1016/S0997-7538(01)01147-0

Bessa, M.A., Bostanabad, R., Liu, Z., Hu, A., Apley, D.W., Brinson, C., Chen, W., Liu, W.K., 2017. A framework for data-driven analysis of materials under uncertainty: Countering the curse of dimensionality. Computer Methods in Applied Mechanics and Engineering 320, 633–667. https://doi.org/10.1016/j.cma.2017.03.037

Bessa, M.A., Pellegrino, S., 2018. Design of ultra-thin shell structures in the stochastic post-buckling range using Bayesian machine learning and optimization. International Journal of Solids and Structures 139–140, 174–188. https://doi.org/10.1016/j.ijsolstr.2018.01.035

Bonatti, C., Mohr, D., 2022. On the importance of self-consistency in recurrent neural network models representing elasto-plastic solids. Journal of the Mechanics and Physics of Solids 158, 104697. https://doi.org/10.1016/j.jmps.2021.104697

Bonatti, C., Mohr, D., 2021. One for all: Universal material model based on minimal state-space neural networks. Science Advances 7, eabf3658. https://doi.org/10.1126/sciadv.abf3658

Brünig, M., Chyra, O., Albrecht, D., Driemeier, L., Alves, M., 2008. A ductile damage criterion at various stress triaxialities. International Journal of Plasticity 24, 1731–1755. https://doi.org/10.1016/j.ijplas.2007.12.001

Brünig, M., Gerke, S., Hagenbrock, V., 2013. Micro-mechanical studies on the effect of the stress triaxiality and the Lode parameter on ductile damage. International Journal of Plasticity 50, 49–65. https://doi.org/10.1016/j.ijplas.2013.03.012

Cazacu, O., Plunkett, B., Barlat, F., 2006. Orthotropic yield criterion for hexagonal closed packed metals. International Journal of Plasticity 22, 1171–1194. https://doi.org/10.1016/j.ijplas.2005.06.001

Choi, S.-W., Jeong, J.S., Won, J.W., Hong, J.K., Choi, Y.S., 2021. Grade-4 commercially pure titanium with ultrahigh strength achieved by twinning-induced grain refinement through cryogenic deformation. Journal of Materials Science & Technology 66, 193–201. https://doi.org/10.1016/j.jmst.2020.04.082

Chu, C.C., Needleman, A., 1980. Void Nucleation Effects in Biaxially Stretched Sheets. Journal of Engineering Materials and Technology 102, 249–256. https://doi.org/10.1115/1.3224807

Clift, S.E., Hartley, P., Sturgess, C.E.N., Rowe, G.W., 1990. Fracture prediction in plastic deformation processes. International Journal of Mechanical Sciences 32, 1–17. https://doi.org/10.1016/0020-7403(90)90148-C

Deguchi, M., Yamasaki, S., Mitsuhara, M., Nakashima, H., Tsukamoto, G., Kunieda, T., 2023. Tensile Deformation Behaviors of Pure Ti with Different Grain Sizes under Wide-Range of Strain Rate. Materials 16, 529. https://doi.org/10.3390/ma16020529

Deng, N., Kuwabara, T., Korkolis, Y.P., 2015. Cruciform Specimen Design and Verification for Constitutive Identification of Anisotropic Sheets. Exp Mech 55, 1005–1022. https://doi.org/10.1007/s11340-015-9999-y

Dunand, M., Maertens, A.P., Luo, M., Mohr, D., 2012. Experiments and modeling of anisotropic aluminum extrusions under multi-axial loading – Part I: Plasticity. International Journal of Plasticity 36, 34–49. https://doi.org/10.1016/j.ijplas.2012.03.003

Dunand, M., Mohr, D., 2010. Hybrid experimental–numerical analysis of basic ductile fracture experiments for sheet metals. International Journal of Solids and Structures 47, 1130–1143. https://doi.org/10.1016/j.ijsolstr.2009.12.011

Fazily, P., Yoon, J.W., 2023. Machine learning-driven stress integration method for anisotropic plasticity in sheet metal forming. International Journal of Plasticity 166, 103642. https://doi.org/10.1016/j.ijplas.2023.103642

Feng, Z., Mamros, E.M., Ha, J., Kinsey, B.L., Knezevic, M., 2021. Modeling of plasticity-induced martensitic transformation to achieve hierarchical, heterogeneous, and tailored microstructures in stainless steels. CIRP Journal of Manufacturing Science and Technology 33, 389–397. https://doi.org/10.1016/j.cirpj.2021.04.006

Gologanu, M., Leblond, J.-B., Devaux, J., 1993. Approximate models for ductile metals containing non-spherical voids—Case of axisymmetric prolate ellipsoidal cavities. Journal of the Mechanics and Physics of Solids 41, 1723–1754. https://doi.org/10.1016/0022-5096(93)90029-F

Gorji, M.B., Mozaffar, M., Heidenreich, J.N., Cao, J., Mohr, D., 2020. On the potential of recurrent neural networks for modeling path dependent plasticity. Journal of the Mechanics and Physics of Solids 143, 103972. https://doi.org/10.1016/j.jmps.2020.103972

Grange, M., Besson, J., Andrieu, E., 2000. An anisotropic Gurson type model to represent the ductile rupture of hydrided Zircaloy-4 sheets [WWW Document]. URL https://www.proquest.com/docview/2259851690?parentSessionId=Y%2FSwWUhAXJAIz%2BncCSLqrR9KX6Pz7%2BcKAxZiLLR%2BZoI%3D (accessed 7.25.23).

Gurland, J., 1972. Observations on the fracture of cementite particles in a spheroidized 1.05% c steel deformed at room temperature. Acta Metallurgica 20, 735–741. https://doi.org/10.1016/0001-6160(72)90102-2

Gurson, A.L., 1977. Continuum Theory of Ductile Rupture by Void Nucleation and Growth: Part I—Yield Criteria and Flow Rules for Porous Ductile Media. Journal of Engineering Materials and Technology 99, 2–15. https://doi.org/10.1115/1.3443401

Ha, J., Baral, M., Korkolis, Y.P., 2019a. Ductile fracture of an aluminum sheet under proportional loading. Journal of the Mechanics and Physics of Solids 132, 103685. https://doi.org/10.1016/j.jmps.2019.103685

Ha, J., Baral, M., Korkolis, Y.P., 2019b. Ductile fracture of an aluminum sheet under proportional loading. Journal of the Mechanics and Physics of Solids 132, 103685. https://doi.org/10.1016/j.jmps.2019.103685

Ha, J., Baral, M., Korkolis, Y.P., 2018. Plastic anisotropy and ductile fracture of bake-hardened AA6013 aluminum sheet. International Journal of Solids and Structures 155, 123–139. https://doi.org/10.1016/j.ijsolstr.2018.07.015

Ha, J., Coppieters, S., Korkolis, Y.P., 2020. On the expansion of a circular hole in an orthotropic elastoplastic thin sheet. International Journal of Mechanical Sciences 182, 105706. https://doi.org/10.1016/j.ijmecsci.2020.105706

Ha, J., Korkolis, Y.P., 2021. Hole-Expansion: Sensitivity of Failure Prediction on Plastic Anisotropy Modeling. JMMP 5, 28. https://doi.org/10.3390/jmmp5020028

Habib, S.A., Lloyd, J.T., Meredith, C.S., Khan, A.S., Schoenfeld, S.E., 2019. Fracture of an anisotropic rare-earth-containing magnesium alloy (ZEK100) at different stress states and strain rates: Experiments and modeling. International Journal of Plasticity 122, 285–318. https://doi.org/10.1016/j.ijplas.2019.07.011

Hayden, H.W., Floreen, S., 1969. Observations of localized deformation during ductile fracture. Acta Metallurgica 17, 213–224. https://doi.org/10.1016/0001-6160(69)90060-1

Hu, Q., Yoon, J.W., Manopulo, N., Hora, P., 2021. A coupled yield criterion for anisotropic hardening with analytical description under associated flow rule: Modeling and validation. International Journal of Plasticity 136, 102882. https://doi.org/10.1016/j.ijplas.2020.102882

Ishiki, M., Kuwabara, T., Hayashida, Y., 2011. Measurement and analysis of differential work hardening behavior of pure titanium sheet using spline function. Int J Mater Form 4, 193–204. https://doi.org/10.1007/s12289-010-1024-5

Jang, D.P., Fazily, P., Yoon, J.W., 2021. Machine learning-based constitutive model for J2- plasticity. International Journal of Plasticity 138, 102919. https://doi.org/10.1016/j.ijplas.2020.102919

Johnson, G.R., Cook, W.H., 1985. Fracture characteristics of three metals subjected to various strains, strain rates, temperatures and pressures. Engineering Fracture Mechanics 21, 31–48. https://doi.org/10.1016/0013-7944(85)90052-9

Jordan, B., Gorji, M.B., Mohr, D., 2020. Neural network model describing the temperature- and rate-dependent stress-strain response of polypropylene. International Journal of Plasticity 135, 102811. https://doi.org/10.1016/j.ijplas.2020.102811

Khan, A.S., Liu, H., 2012a. A new approach for ductile fracture prediction on Al 2024-T351 alloy. International Journal of Plasticity 35, 1–12. https://doi.org/10.1016/j.ijplas.2012.01.003

Khan, A.S., Liu, H., 2012b. Strain rate and temperature dependent fracture criteria for isotropic and anisotropic metals. International Journal of Plasticity 37, 1–15. https://doi.org/10.1016/j.ijplas.2012.01.012

Khan, A.S., Yu, S., Liu, H., 2012. Deformation induced anisotropic responses of Ti–6Al–4V alloy Part II: A strain rate and temperature dependent anisotropic yield criterion. International Journal of Plasticity 38, 14–26. https://doi.org/10.1016/j.ijplas.2012.03.013

Kim, J., Ebrahim, A.S., Kinsey, B.L., Ha, J., 2024. Identification of Yld2000–2d anisotropic yield function parameters from single hole expansion test using machine learning. CIRP Annals S0007850624000349. https://doi.org/10.1016/j.cirp.2024.04.026

Le Roy, G., Embury, J.D., Edwards, G., Ashby, M.F., 1981. A model of ductile fracture based on the nucleation and growth of voids. Acta Metallurgica 29, 1509–1522. https://doi.org/10.1016/0001-6160(81)90185-1

Lebensohn, R.A., Tomé, C.N., 1993. A self-consistent anisotropic approach for the simulation of plastic deformation and texture development of polycrystals: Application to zirconium alloys. Acta Metallurgica et Materialia 41, 2611–2624. https://doi.org/10.1016/0956-7151(93)90130-K

Lebensohn, R.A., Tomé, C.N., CastaÑeda, P.P., 2007. Self-consistent modelling of the mechanical behaviour of viscoplastic polycrystals incorporating intragranular field fluctuations. Philosophical Magazine 87, 4287–4322. https://doi.org/10.1080/14786430701432619

Leblond, J., Perrin, G., Devaux, J., 1995. An improved Gurson-type model for hardenable ductile metals. European Journal of Mechanics A-solids.

Lee, J., Bong, H.J., Ha, J., 2022. Efficient and robust stress integration algorithm for anisotropic distortional hardening law under cross-loading with latent hardening. European Journal of Mechanics - A/Solids 96, 104775. https://doi.org/10.1016/j.euromechsol.2022.104775

Lee, J., Bong, H.J., Ha, J., Choi, J., Barlat, F., Lee, M.-G., 2018. Influence of Yield Stress Determination in Anisotropic Hardening Model on Springback Prediction in Dual-Phase Steel. JOM 70, 1560–1566. https://doi.org/10.1007/s11837-018-2910-4

Lee, J., Ha, J., Bong, H.J., Kim, D., Lee, M.-G., 2016. Evolutionary anisotropy and flow stress in advanced high strength steels under loading path changes. Materials Science and Engineering: A 672, 65–77. https://doi.org/10.1016/j.msea.2016.06.074

Lee, J.-W., Lee, M.-G., Barlat, F., 2012. Finite element modeling using homogeneous anisotropic hardening and application to spring-back prediction. International Journal of Plasticity 29, 13–41. https://doi.org/10.1016/j.ijplas.2011.07.007

Li, X., Christian, C., Mohr, D., 2023. Neural Network Based Rate- and Temperature-Dependent Hosford-Coulomb Fracture Initiation Model. International Journal of Mechanical Sciences 108643. https://doi.org/10.1016/j.ijmecsci.2023.108643

Li, X., Roth, C.C., Bonatti, C., Mohr, D., 2022. Counterexample-trained neural network model of rate and temperature dependent hardening with dynamic strain aging. International Journal of Plasticity 151, 103218. https://doi.org/10.1016/j.ijplas.2022.103218

Li, X., Roth, C.C., Mohr, D., 2019. Machine-learning based temperature- and rate-dependent plasticity model: Application to analysis of fracture experiments on DP steel. International Journal of Plasticity 118, 320–344. https://doi.org/10.1016/j.ijplas.2019.02.012

Li, Y., Luo, M., Gerlach, J., Wierzbicki, T., 2010. Prediction of shear-induced fracture in sheet metal forming. Journal of Materials Processing Technology 210, 1858–1869. https://doi.org/10.1016/j.jmatprotec.2010.06.021

Li, Y., Wierzbicki, T., 2010. Prediction of plane strain fracture of AHSS sheets with post-initiation softening. International Journal of Solids and Structures 47, 2316–2327. https://doi.org/10.1016/j.ijsolstr.2010.04.028

Liao, K.-C., Pan, J., Tang, S.C., 1997. Approximate yield criteria for anisotropic porous ductile sheet metals. Mechanics of Materials 26, 213–226. https://doi.org/10.1016/S0167-6636(97)00033-1

Liu, X., He, J., Huang, S., 2023. Mechanistically informed artificial neural network model for discovering anisotropic path-dependent plasticity of metals. Materials & Design 226, 111697. https://doi.org/10.1016/j.matdes.2023.111697

Lou, Y., Yoon, J.W., 2017. Anisotropic ductile fracture criterion based on linear transformation. International Journal of Plasticity 93, 3–25. https://doi.org/10.1016/j.ijplas.2017.04.008

Lou, Y., Yoon, J.W., Huh, H., 2014. Modeling of shear ductile fracture considering a changeable cut-off value for stress triaxiality. International Journal of Plasticity 54, 56–80. https://doi.org/10.1016/j.ijplas.2013.08.006

Luo, M., Dunand, M., Mohr, D., 2012. Experiments and modeling of anisotropic aluminum extrusions under multi-axial loading – Part II: Ductile fracture. International Journal of Plasticity 32–33, 36–58. https://doi.org/10.1016/j.ijplas.2011.11.001

Mamros, E.M., Mayer, S.M., Banerjee, D.K., Iadicola, M.A., Kinsey, B.L., Ha, J., 2022. Plastic anisotropy evolution of SS316L and modeling for novel cruciform specimen. International Journal of Mechanical Sciences 234, 107663. https://doi.org/10.1016/j.ijmecsci.2022.107663

McClintock, F.A., 1968. A Criterion for Ductile Fracture by the Growth of Holes. Journal of Applied Mechanics 35, 363–371. https://doi.org/10.1115/1.3601204

Meng, W., Zhu, H., Wang, X., Li, G., Fan, Y., Sun, D., Kong, F., 2022. Electrochemical Behavior and Surface Conductivity of C/TiC Nanocomposite Coating on Titanium for PEMFC Bipolar Plate. Metals 12, 771. https://doi.org/10.3390/met12050771

Mirone, G., Corallo, D., 2010. A local viewpoint for evaluating the influence of stress triaxiality and Lode angle on ductile failure and hardening. International Journal of Plasticity 26, 348–371. https://doi.org/10.1016/j.ijplas.2009.07.006

Mohr, D., Henn, S., 2007. Calibration of Stress-triaxiality Dependent Crack Formation Criteria: A New Hybrid Experimental–Numerical Method. Exp Mech 47, 805–820. https://doi.org/10.1007/s11340-007-9039-7

Mohr, D., Marcadet, S.J., 2015. Micromechanically-motivated phenomenological Hosford–Coulomb model for predicting ductile fracture initiation at low stress triaxialities. International Journal of Solids and Structures 67–68, 40–55. https://doi.org/10.1016/j.ijsolstr.2015.02.024

Mozaffar, M., Bostanabad, R., Chen, W., Ehmann, K., Cao, J., Bessa, M.A., 2019. Deep learning predicts path-dependent plasticity. Proc. Natl. Acad. Sci. U.S.A. 116, 26414–26420. https://doi.org/10.1073/pnas.1911815116

Mu, L., Jia, Z., Ma, Z., Shen, F., Sun, Y., Zang, Y., 2020. A theoretical prediction framework for the construction of a fracture forming limit curve accounting for fracture pattern transition. International Journal of Plasticity 129, 102706. https://doi.org/10.1016/j.ijplas.2020.102706

Muhammad, W., Brahme, A.P., Ibragimova, O., Kang, J., Inal, K., 2021. A machine learning framework to predict local strain distribution and the evolution of plastic anisotropy & fracture in additively manufactured alloys. International Journal of Plasticity 136, 102867. https://doi.org/10.1016/j.ijplas.2020.102867

Mutrus, A., Hora, P., Peters, P., Tong, L., 2010. Modeling of anisotropic hardening behavior based on the Yld2000 yield locus description.

Nagano, C., Kuwabara, T., Shimada, Y., Kawamura, R., 2018. Measurement of Differential Hardening under Biaxial Stress of Pure Titanium Sheet. IOP Conf. Ser.: Mater. Sci. Eng. 418, 012090. https://doi.org/10.1088/1757-899X/418/1/012090

Oh, S.I., Chen, C.C., Kobayashi, S., 1979. Ductile Fracture in Axisymmetric Extrusion and Drawing—Part 2: Workability in Extrusion and Drawing. Journal of Engineering for Industry 101, 36–44. https://doi.org/10.1115/1.3439471

Ortiz, M., Simo, J.C., 1986. An analysis of a new class of integration algorithms for elastoplastic constitutive relations. Numerical Meth Engineering 23, 353–366. https://doi.org/10.1002/nme.1620230303

Pandya, K.S., Roth, C.C., Mohr, D., 2020. Strain rate and temperature dependent fracture of aluminum alloy 7075: Experiments and neural network modeling. International Journal of Plasticity 135, 102788. https://doi.org/10.1016/j.ijplas.2020.102788

Pardoen, T., Hutchinson, J.W., 2000. An extended model for void growth and coalescence. Journal of the Mechanics and Physics of Solids 48, 2467–2512. https://doi.org/10.1016/S0022-5096(00)00019-3

Peng, Z., Zhao, H., Li, X., 2021. New ductile fracture model for fracture prediction ranging from negative to high stress triaxiality. International Journal of Plasticity 145, 103057. https://doi.org/10.1016/j.ijplas.2021.103057

Peters, P., Manopulo, N., Lange, C., Hora, P., 2014. A strain rate dependent anisotropic hardening model and its validation through deep drawing experiments. Int J Mater Form 7, 447–457. https://doi.org/10.1007/s12289-013-1140-0

Pham, Q.T., Lee, M.G., Kim, Y.S., 2019. Characterization of the isotropic-distortional hardening model and its application to commercially pure titanium sheets. International Journal of Mechanical Sciences 160, 90–102. https://doi.org/10.1016/j.ijmecsci.2019.06.023

Rice, J.R., Tracey, D.M., 1969. On the ductile enlargement of voids in triaxial stress fields∗. Journal of the Mechanics and Physics of Solids 17, 201–217. https://doi.org/10.1016/0022-5096(69)90033-7

Roth, A., Lebyodkin, M.A., Lebedkina, T.A., Lecomte, J.-S., Richeton, T., Amouzou, K.E.K., 2014. Mechanisms of anisotropy of mechanical properties of α-titanium in tension conditions. Materials Science and Engineering: A 596, 236–243. https://doi.org/10.1016/j.msea.2013.12.061

Roth, C.C., Mohr, D., 2018. Determining the strain to fracture for simple shear for a wide range of sheet metals. International Journal of Mechanical Sciences 149, 224–240. https://doi.org/10.1016/j.ijmecsci.2018.10.007

Roth, C.C., Mohr, D., 2016. Ductile fracture experiments with locally proportional loading histories. International Journal of Plasticity 79, 328–354. https://doi.org/10.1016/j.ijplas.2015.08.004

Schmidt, J., Hartmaier, A., 2023. A new texture descriptor for data-driven constitutive modeling of anisotropic plasticity. J Mater Sci 58, 14029–14050. https://doi.org/10.1007/s10853-023-08852-2

Tasdemir, B., Tagarielli, V., Pellegrino, A., 2023. A data-driven model of the yield and strain hardening response of commercially pure titanium in uniaxial stress. Materials & Design 229, 111878. https://doi.org/10.1016/j.matdes.2023.111878

Tvergaard, V., Needleman, A., 1984. Analysis of the cup-cone fracture in a round tensile bar. Acta Metallurgica 32, 157–169. https://doi.org/10.1016/0001-6160(84)90213-X

Van Den Boogaard, T., Havinga, J., Belin, A., Barlat, F., 2016. Parameter reduction for the Yld2004-18p yield criterion. Int J Mater Form 9, 175–178. https://doi.org/10.1007/s12289-015-1221-3

Wang, H., Wu, P.D., Wang, J., Tomé, C.N., 2013. A crystal plasticity model for hexagonal close packed (HCP) crystals including twinning and de-twinning mechanisms. International Journal of Plasticity 49, 36–52. https://doi.org/10.1016/j.ijplas.2013.02.016

Wang, K., Luo, M., Wierzbicki, T., 2014. Experiments and modeling of edge fracture for an AHSS sheet. Int J Fract 187, 245–268. https://doi.org/10.1007/s10704-014-9937-5

Weber, P., Wagner, W., Freitag, S., 2023. Physically enhanced training for modeling rate-independent plasticity with feedforward neural networks. Comput Mech. https://doi.org/10.1007/s00466-023-02316-9

Wen, J., Huang, Y., Hwang, K., Liu, C., Li, M., 2005. The modified Gurson model accounting for the void size effect. International Journal of Plasticity - INT J PLASTICITY 21, 381–395. https://doi.org/10.1016/j.ijplas.2004.01.004

Wierzbicki, T., Bao, Y., Lee, Y.-W., Bai, Y., 2005. Calibration and evaluation of seven fracture models. International Journal of Mechanical Sciences, A Special Issue in Honour of Professor Stephen R. Reid’s 60th Birthday 47, 719–743. https://doi.org/10.1016/j.ijmecsci.2005.03.003

Wilson, J.F., Kinsey, B.L., Korkolis, Y.P., 2013. Development of a biaxial loading frame for sheet metal. Journal of Manufacturing Processes 15, 580–585. https://doi.org/10.1016/j.jmapro.2013.06.008

Yang, H., Li, H., Sun, H., Zhang, Y.H., Liu, X., Zhan, M., Liu, Y.L., Fu, M.W., 2022. Anisotropic plasticity and fracture of alpha titanium sheets from cryogenic to warm temperatures. International Journal of Plasticity 156, 103348. https://doi.org/10.1016/j.ijplas.2022.103348

Yi, N., Hama, T., Kobuki, A., Fujimoto, H., Takuda, H., 2016. Anisotropic deformation behavior under various strain paths in commercially pure titanium Grade 1 and Grade 2 sheets. Materials Science and Engineering: A 655, 70–85. https://doi.org/10.1016/j.msea.2015.12.081

Zhai, J., Luo, T., Gao, X., Graham, S.M., Baral, M., Korkolis, Y.P., Knudsen, E., 2016. Modeling the ductile damage process in commercially pure titanium. International Journal of Solids and Structures 91, 26–45. https://doi.org/10.1016/j.ijsolstr.2016.04.031

Zhang, A., Mohr, D., 2020. Using neural networks to represent von Mises plasticity with isotropic hardening. International Journal of Plasticity 132, 102732. https://doi.org/10.1016/j.ijplas.2020.102732

Zheng, L., Wang, Z., Meng, B., Wan, M., 2023. A unified ductile fracture criterion suitable for sheet and bulk metals considering multiple void deformation modes. International Journal of Plasticity 164, 103572. https://doi.org/10.1016/j.ijplas.2023.103572

CRediT statement

A.S. Ebrahim: Data curation; Formal analysis; Investigation; Software; Validation; Visualization; Writing - original draft

Q. Zhang: Methodology; Software; Supervision;

J. Ha: Conceptualization; Funding acquisition; Methodology; Supervision; Writing - review & editing

No conflict of interest to report. See the document for declaration of interest statement.

Declaration of interests

☒ The authors declare that they have no known competing financial interests or personal relationships that could have appeared to influence the work reported in this paper.

☐ The authors declare the following financial interests/personal relationships which may be considered as potential competing interests: